Monthly Notices of the ROYAL ASTRONOMICAL SOCIETY

MNRAS **548,** 1–29 (2026) https://doi.org/10.1093/mnras/stag733
Advance Access publication 2026 April 20

Infrared spectral signatures of light *r*-process elements in kilonovae

Anders Jerkstrand [1]★ Quentin Pognan [2] Smaranika Banerjee [1,3] Nicholas C. Sterling [4] Jon Grumer [5] Niamh Ferguson [6] Keith Butler,[7] James Gillanders [8] Stephen Smartt [8] Kyohei Kawaguchi [2,9] and Blanka Vilagos [1]

[1]*The Oskar Klein Centre, Department of Astronomy, Stockholm University, AlbaNova, SE-10691 Stockholm, Sweden*
[2]*Max Planck Institute for Gravitational Physics (Albert Einstein Institute), Am Mühlenberg 1, Potsdam-Golm D-14476, Germany*
[3]*Institut für Kernphysik, Technische Universität Darmstadt, Schlossgartenstr. 2, D-64289 Darmstadt, Germany*
[4]*University of West Georgia, 1601 Maple Street, Carrollton, GA 30118, USA*
[5]*Theoretical Astrophysics, Department of Physics and Astronomy, Uppsala University, Box 516, SE-751 20 Uppsala, Sweden*
[6]*Department of Physics, University of Strathclyde, Glasgow G4 0NG, UK*
[7]*Ludwig-Maximilians-Universität München, Universitätssternwarte, Scheinerstr. 1, 81679 München, Germany*
[8]*Astrophysics sub-Department, Department of Physics, University of Oxford, Keble Road, Oxford OX1 3RH, UK*
[9]*Center of Gravitational Physics and Quantum Information, Yukawa Institute for Theoretical Physics, Kyoto University, Kyoto 606-8502, Japan*

Accepted 2026 April 8. Received 2026 March 20; in original form 2025 October 10

ABSTRACT

A central question regarding neutron star (NS) mergers is whether they are able to produce all the *r*-process elements, from first to third peak. We here study theoretical infrared signatures of first-peak elements with spectral synthesis modelling. By combining state-of-the-art non-local thermodynamic equilibrium physics with new radiative and collisional data for these elements, we identify several promising diagnostic lines from Ge, As, Se, Br, Kr, and Zr. The models give self-consistent line luminosities and indicate specific features that probe emission volumes at early phases ($\sim$10 d), the product of ion mass and electron density in late phases ($\gtrsim$75 d), and in some cases direct ionic masses at intermediate phases. Emission by [Se I] 5.03 μm + [Se III] 4.55 μm is the only candidate from the first *r*-process peak that could explain the *Spitzer* photometry of AT2017gfo. However, the models show consistently that with a Kr/Te and Se/Te ratio following the solar *r*-process pattern, Kr + Se emission is dominant over Te for the feature at 2.1 μm observed in both AT2017gfo and AT2023vfi. The somewhat better line profile fit with [Te III] may suggest that both AT2017gfo and AT2023vfi had a strongly subsolar production of the light *r*-process elements. An alternative scenario could be that Kr + Se in an asymmetric morphological distribution generates the feature. Further *James Webb Space Telescope* spectral observations hold promise to determine the light *r*-process production of kilonovae, and in particular whether the light elements are made in a slow disc outflow or in a fast proto-NS wind. We identify specific needs for further atomic data for $Z = 31 - 40$ elements.

Key words: line: formation – line: identification – radiative transfer – supernovae: general – nuclear reactions, nucleosynthesis, abundances.

1 INTRODUCTION

The *James Webb Space Telescope* (*JWST*) is currently revolutionizing many branches of astronomy, opening up the near-infrared (NIR) and mid-infrared (MIR) regimes which can now be studied with excellent sensitivity and spectral resolution. For explosive transients, such as supernovae (SNe) and kilonovae (KNe), the IR contains rich signatures of atomic transitions that are often less affected by uncertain physical conditions than optical lines. While the *Spitzer Space Telescope* revealed much information about Type II SNe (R. Kotak et al. 2006, 2009), other SN types were not observed. The first KN, AT2017gfo, was photometrically detected in the *Spitzer* warm phase (M. M. Kasliwal et al. 2022). However, it is *JWST,* and in a few years the *Extremely Large Telescope*, that will give us detailed spectral information about these transients in the IR.

The importance of the IR regime for trans-iron elements has been established in studies of planetary nebulae (PNe). The first detection of neutron-capture elements in a PN, or any type of nebula, was the detection of optical Kr and Xe lines by D. Pequignot & J. P. Baluteau (1994). The NIR range subsequently yielded detections of [Kr III] 2.199 μm and [Se IV] 2.287 μm (H. L. Dinerstein 2001), [Zn IV] 3.625 μm (H. L. Dinerstein & T. R. Geballe 2001), [Rb IV] 1.5973 μm, [Cd IV] 1.7204 μm, [Ge VI] 2.1930 μm (N. C. Sterling et al. 2016), [Br V] 1.6429 μm, [Te III] 2.1019 μm (S. Madonna et al. 2018), and [Rb III] 1.356 μm (H. L. Dinerstein et al. 2021). These detections prompted work to develop the needed atomic data for these elements to carry out abundance analyses (e.g. N. C. Sterling 2011; N. C. Sterling & M. C. Witthoeft

★ E-mail: anders.jerkstrand@astro.su.se

2011; N. C. Sterling, R. L. Porter & H. L. Dinerstein 2015; B. M. McLaughlin & J. F. Babb 2019; D. A. Macaluso et al. 2019). The post-diffusion phase ($t \gtrsim 1$ week for KNe) gives unique information about explosive transients as the innermost layers, typically containing most of the ejecta mass, become visible as the nebula becomes more transparent. With radiative transfer playing a smaller role, and Doppler broadening being smaller for the inner layers, spectral signatures emerge more cleanly than in the diffusion phase. At the same time, modelling of the physical conditions becomes more challenging, as the necessary abandonment of local thermodynamic equilibrium (LTE) for full non-LTE (NLTE) collisional radiative modelling brings about sensitivity to a large variety of collisional and radiative processes (see e.g. A. Jerkstrand 2025, for a review), and requires an extensive computational machinery. For KNe, comprehensive NLTE modelling work has been done by K. Hotokezaka et al. (2021, 2022, 2023, simplified NLTE in the optically thin limit) and by Q. Pognan, A. Jerkstrand & J. Grumer (2022a, b); Q. Pognan et al. (2023, 2025, full NLTE with radiative transfer). The impact of recombination rates on NLTE ionization and spectra was studied by S. Banerjee et al. (2025), and a study of how NLTE ionization effects depend on density and temperature at early phases was carried out by D. Brethauer et al. (2026). Y. Tarumi et al. (2023) and A. Sneppen et al. (2024) have studied NLTE effects on He line formation.

What is looked for in nebular analysis are signatures that, based on inspection of the line formation mechanisms, can be established as diagnostics with good robustness (i.e. not too sensitive to physical conditions or uncertain physics or parameters). In this endeavour, the IR is a particularly potent regime. Under typical nebular plasma conditions, IR lines often originate from forbidden transitions within the ground term of a given ion, and with the relatively small excitation energies ($T_{exc} \lesssim 2000\,(\lambda/2\ \mu m)^{-1}$ K), the line luminosities can be in a quite temperature-insensitive regime (if $T \gtrsim T_{\rm exc}$). Further, as transitions between fine structure states of a given term tend to have small A-values and large collision strengths, the critical densities for them are quite low and they can be close to LTE for quite long times, giving no or weak sensitivity to the electron density. Finally, line opacity generally declines with wavelength, so there are no or weak radiative transfer effects. What results from these properties is that IR lines are excellent diagnostics of ionic masses (optically thin case) and/or emission volume (optically thick case) (S. H. Moseley et al. 1989; M. R. Haas et al. 1990; D. H. Wooden et al. 1993; A. Jerkstrand et al. 2012; A. Jerkstrand 2017).

These benign properties of the IR regime give expectations of strong scientific return with *JWST* for explosive transients. Extending the observable limit from up to 2.5 μm (accessible from the ground) to 30 μm, and with excellent sensitivity, *JWST* is expected to be able to reveal key spectral signatures of KNe and other transients. It has already shown its value by the observations of IR emission of the presumed KN AT2023vfi at a distance of 292 Mpc (A. J. Levan et al. 2024).

With these prospects, it is imperative to improve our theoretical understanding of KN IR emission, and to develop model predictions for a variety of compact object merger types. This topic was opened up by K. Hotokezaka et al. (2021), who studied nebular spectral emission by neodymium, including in the IR. K. Hotokezaka et al. (2022) produced theoretical predictions of IR emission from solar composition ejecta with fixed parametrized physical conditions (temperature and ionization), in a limited NLTE approach (thermal collisions and spontaneous radiative decay included). The strongest emission was obtained for [Se III] 5.74 μm, whereas the *Spitzer* 4.5 and 3.6 μm bands were found to be dominated by [Se III] 4.55 and Br + As lines, respectively.

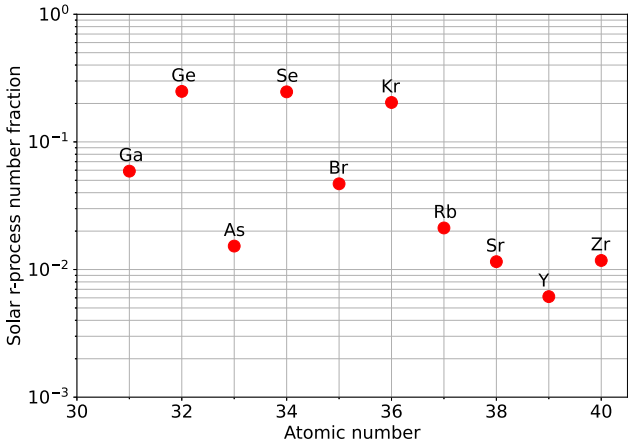

Figure 1. The solar '*r*-process' (i.e. non *s*-process) number abundances in the $Z = 31 - 40$ range, according to the N. Prantzos et al. (2020) estimation. The value for Te ($Z = 52$, not plotted) is 2.3 per cent.

From this exploratory modelling, the next step is modelling with calculation of physical conditions, with some consideration of the density structure of the ejecta. This is the main goal of this paper. We have presented the optical (and some NIR) properties of 1D full NLTE spectral models in Q. Pognan et al. (2022a, 2023) – here the focus is on the NIR and MIR emission of models with a similar setup. With the importance of accurate atomic physics, we have adopted an approach to initially limit the focus to the IR emission from light *r*-process elements only, $Z \leq 40$ [with one exception, Te ($Z = 52$), due to its possible identification in observed spectra], carrying out an extensive atomic data compilation and calibration effort for these elements. Complementary information regarding the impact of lanthanides is presented in Q. Pognan et al. (2026).

2 MODELLING SETUP

The goal of the study is to establish an orientation of the nebular NIR and MIR signatures of light *r*-process elements in KN ejecta, being aided by self-consistent physical NLTE modelling. We use the SUMO code (A. Jerkstrand, C. Fransson & C. Kozma 2011; A. Jerkstrand et al. 2012), adopting a 1D approach where our base-line model is similar to the models in Q. Pognan et al. (2023). Because the light *r*-process elements ($31 \leq Z \leq 40$) make up about 80 per cent of the solar *r*-process composition by mass (and 87 per cent by number, Fig. 1, N. Prantzos et al. 2020), it is plausible that the ejecta of many KNe are dominated by these elements. The ejecta mass of AT2017gfo has been estimated to be about 0.05 $M_\odot$ (e.g. S. J. Smartt et al. 2017; V. A. Villar et al. 2017; M. Tanaka et al. 2017; R. T. Wollaeger et al. 2018; N. Vieira et al. 2025), which is the value we use for the model ejecta here.

Light *r*-process elements are made in significant amounts in regions where the electron fraction Y_e (number of protons relative to number of nucleons) is raised to $\gtrsim 0.3$ due to positron capture and neutrino irradiation. In current simulations, dynamic, secular (disc outflow), and hypermassive neutron star (HMNS) polar wind components can all have parts with such conditions (e.g. S. Wanajo et al. 2014; S. Goriely et al. 2015; S. Fujibayashi et al. 2020b; O. Just et al. 2023; S. Curtis et al. 2023). However, only

the disc outflow component reaches, in current simulations, the kind of masses inferred for AT2017gfo (and one may also note that ejecta mass was likely yet larger in AT2023vfi, J. C. Rastinejad et al. 2025). It is therefore reasonable to associate the baseline model with such ejecta. The disc outflow can achieve high Y_e values ($\gtrsim 0.2$) due to positron capture (e.g. R. Fernández & B. D. Metzger 2013; S. Fujibayashi et al. 2020a; O. Just et al. 2022) or even values as high as 0.4–0.5 via neutrino irradiation by either an HMNS (B. D. Metzger & R. Fernández 2014) or the disc itself (O. Just et al. 2015, 2023).

The density profiles of various high-Y_e components can vary, both between simulations and within a simulation with position angle. The analytic limit for a disc wind is a -2 power law, whereas other components can be steeper, roughly described by -3 or -4 power laws (e.g. K. Kawaguchi et al. 2021; O. Just et al. 2022; R. Fernández et al. 2024). We use a -3 power law throughout as a value that lies relatively close to all scenarios.

The mean velocity of a disc outflow is significantly lower than for dynamic ejecta or HMNS outflows, although with magnetohydrodynamic effects the difference is somewhat reduced (K. Kiuchi et al. 2023). We choose an inner boundary velocity $v_{in} = 0.02c$ to obtain mean velocities ($\langle\beta = v/c\rangle = 0.078$ for a -3 power law) roughly consistent with disc outflow simulations (e.g. $\langle\beta\rangle \sim 0.05$ in the simulations of O. Just et al. 2023), but a higher value $v_{in} = 0.08c$ (giving $\langle\beta\rangle = 0.13$ for a -3 power law) in an alternative model which would correspond closer to the other components (e.g. $\beta = 0.1 - 0.2$ for the proto-NS wind in the simulations of O. Just et al. 2023). The ejecta are terminated at $v_{out} = 0.2c$, with material faster than this playing a subdominant role at nebular phases.

The abundances are set to the solar *r*-process pattern for $Z = 31 - 40$ and 52, as estimated by N. Prantzos et al. (2020), plus 1 per cent abundance each (by mass) of Fe, Ni, and Zn. Although the study is focused on the $Z \leq 40$ elements, Te ($Z = 52$) was added due to its possible identification in both AT2017gfo (K. Hotokezaka et al. 2023) and AT2023vfi (A. J. Levan et al. 2024). Inspection of the detailed abundance patterns in the simulations of K. Kawaguchi et al. (2021), O. Just et al. (2023), S. Fujibayashi et al. (2023), and R. Fernández et al. (2024), shows that the $Z = 34 - 40$ pattern is relatively close to the solar one for most simulations. For $Z = 31 - 33$, there is, however, more variation and simulations tend to produce lower abundances than solar. S. Goriely (1999) assesses the solar *r*-process abundances of $Z = 31$ (Ga) as very uncertain, with potentially a value much lower than the standard one.

All the simulations mentioned above give abundances of $Z = 26, 28, 30$ being the highest in the $Z = 20 - 30$ range, and of order 1 per cent of the $Z = 31 - 40$ total abundance, which we adopt. By using the solar *r*-process abundance distribution the model is made as generic as possible, but still in broad agreement with KN simulations, although not tied to any particular one.

The zoning is done with logarithmic 10 per cent steps in velocity, resulting in of order 20 zones (depending on $v_{\rm in}$ and $v_{\rm out}$). This is an increase compared to the 5 zones used in Q. Pognan et al. (2023), which better spatially resolves the physical conditions and radiative transfer.

Radioactive powering varies significantly with composition (e.g. S. Wanajo et al. 2014) and also with uncertain nuclear physics for fixed Y_e (J. Barnes et al. 2021). KNe have multiple ejecta components, with different Y_e and different morphologies. For this reason, we allow a certain freedom for the power deposition, that is intended to bracket the range of conditions in KNe. The baseline powering, 'low power', has the decay power of a $Y_e = 0.35$ composition (S. Wanajo et al. 2014), whereas 'high power' multiplies this by a factor f. This scenario could represent e.g. a $Z = 30 - 40$ ejecta component exposed to radioactive decay particles from another more neutron-rich composition in the ejecta. We choose an approach where we boost the power in the high-velocity model with a factor $f = 3$. This allows us to probe the likely span of ionization states, with the low-velocity, low-power model giving a quite neutral ejecta, whereas the high-velocity, high-power one gives high ionization (both low-density and high-power work to increase ionization). In this way, we can bracket the range of possible lines from the studied elements. A study of the impact of f is provided in Appendix B.

Thermalization is computed in the same way as in previous papers, with time delay accounted for using the analytic methods of D. Kasen & J. Barnes (2019) and E. Waxman, E. O. Ofek & D. Kushnir (2019), but specific flows into heating and ionization channels (non-thermal excitation is ignored) using the Spencer–Fano routine of SUMO.

The baseline atomic data is the FAC calculation set presented in Q. Pognan et al. (2023). However, we have here also carried out extensive calibrations of energy levels, wavelengths, and *A*-values relevant for IR lines, and also added in new recombination and collision rates, with details outlined in Appendix A. Of particular importance are the new dielectronic recombination rates for light r-process elements computed by S. Banerjee et al. (2025). For collision strengths, computed values are used for several ions. When the values are unknown, we make a separate treatment between forbidden fine-structure lines (most important for this study) and others, because the fine-structure transitions often have significantly larger collision strengths than higher-energy ones. For the first group, we fitted the formula $\Upsilon = \text{const} \times g_u g_l$ (T. S. Axelrod 1980), where g_u and g_l are the statistical weights of upper and lower levels, to all the calculated fine-structure data for the included elements (see Appendix A), obtaining a best-fitting coefficient of const = 0.41. For the others, we used the Axelrod value derived for iron (const = 0.004) boosted by a factor 10 to bring better agreement with recent calculations for trans-iron elements (S. J. Bromley et al. 2023; L. P. Mulholland et al. 2024a, 2025; D. J. Dougan et al. 2025; M. McCann et al. 2025).

We study two models, A and B, with properties summarized in Table 1. We compute the models at 10, 40, and 80 d, in the steady-state approximation (see Q. Pognan et al. 2022a, for an in-depth study of this approximation), at wavelengths from 400 Å to 30 μm.

3 DATA

We will make comparisons of the computed models to observations of AT2017gfo and AT2023vfi.

We will make use of the + 10.4 d spectrum of AT2017gfo presented by E. Pian et al. (2017); specifically, we use the reduced version of the ENGRAVE data release.[1] The spectrum has been corrected for redshift with $z = 0.009843$ (luminosity distance $D_L = 40$ Mpc) and (Milky Way) extinction with $E(B - V) = 0.11$ mag (J. Hjorth et al. 2017; S. J. Smartt et al. 2017). We smooth the spectrum using a 20-bin boxcar.

M. M. Kasliwal et al. (2022) reported on the detection of AT2017gfo in the *Spitzer* 4.5 μm band at +43 and at + 74 d (see also V. A. Villar et al. 2018, for an alternative data reduction). The

[1] http://www.engrave-eso.org/AT2017gfo-Data-Release

Table 1. Summary of the models studied. Both models have $v_{out} = 0.2c$ and -3 power-law density profiles.

Name	Composition	Deposition	$v_{\rm in}$
A	Solar for $Z = 31-40, 52+26, 28, 30$ at 1 per cent	Low ($f = 1$)	0.02
B	Same as A	High ($f = 3$)	0.08

Spitzer observations also gave upper limits in the 3.6 μm band. The reported 4.5 μm band flux at + 43 d is $F_\nu = 6.43 \times 10^{-29}$ erg s^{-1} cm^{-2} Hz^{-1}, which corresponds to

$$F_\lambda = F_\nu \frac{c}{\lambda^2} = = 9.5 \times 10^{-12} \text{ erg s}^{-1}\text{cm}^{-2}\text{cm}^{-1}$$
$$= 9.5 \times 10^{-20} \text{ erg s}^{-1}\text{cm}^{-2}\text{Å}^{-1}. \quad (1)$$

This is equivalent to $F_\lambda \times \lambda_{\mu\rm m} = 4.3 \times 10^{-19}$ erg s^{-1}cm^{-2}Å^{-1} ($\lambda_{\mu m} = 4.5$). We control our conversion by taking

$$L_{\rm band} = F_\lambda \times \Delta\lambda_{\rm band} \times 4\pi d^2$$
$$\approx 9.5 \times 10^{-20} \text{ erg s}^{-1}\text{cm}^{-2}\text{Å}^{-1} \times 10^4 \text{Å} \times 4\pi$$
$$\times \left(40 \times 10^6 \times 3.08 \times 10^{18}\text{cm}\right)^2 = 1.8 \times 10^{38} \text{ erg s}^{-1}, \quad (2)$$

similar to the value 2×10^{38} erg s^{-1} reported in K. Hotokezaka et al. (2022).

The 3.6 μm-band upper limit magnitude at + 43 d of 23.21 corresponds to a flux limit of $F_\nu = 1.9 \times 10^{-29}$ erg s^{-1} cm^{-2} Hz^{-1},[2] or equivalently $F_\lambda \lambda_{\mu m} = 1.6 \times 10^{-19}$ erg s^{-1}cm^{-2}Å^{-1}. For the + 74 d data, the corresponding values in the 4.5 μm band are $F_\nu = 1.04 \times 10^{-29}$ erg s^{-1} cm^{-2} Hz^{-1}, corresponding to $F_\lambda \lambda_{\mu m} = 6.9 \times 10^{-20}$ erg s^{-1}cm^{-2}Å^{-1}. The 3.6 μm band upper limit of 23.05 corresponds to $F_\lambda \lambda_{\mu m} = 1.8 \times 10^{-19}$ erg s^{-1}cm^{-2}Å^{-1}.

We use the *JWST* spectra of GRB 230307A/AT2023vfi, taken at +29 and + 61 d (A. J. Levan et al. 2024), utilizing the reduction of J. H. Gillanders & S. J. Smartt (2025) as our standard set.[3] Different reductions are similar at +29 d, but significantly different at +61 d, for the latter epoch we plot both for completeness. The +29 d spectrum was smoothed with a 3-bin boxcar, and the + 61 d spectrum was smoothed by a 5-bin boxcar. The spectra were corrected for redshift with $z = 0.0646$ (luminosity distance 292 Mpc), and (Milky Way) extinction with $E(B-V) = 0.076$ mag (A. J. Levan et al. 2024). We plot the spectra redward of 1.9 μm, as they are dominated by the Gamma-Ray Burst afterglow blueward of this (see J. H. Gillanders et al. 2023; A. J. Levan et al. 2024; J. H. Gillanders & S. J. Smartt 2025), see also Y.-H. Yang et al. (2024) for complementary afterglow observations and modelling.

4 ANALYTIC LIMITS OF IR LINE FORMATION

Before we proceed to study the model spectra, we review the various analytic limits of nebular line formation (see also A. Jerkstrand 2017).

[2] https://lweb.cfa.harvard.edu/~dfabricant/huchra/ay145/mags.html
[3] The reduced spectra were downloaded from https://ora.ox.ac.uk/objects/uuid:5032f338-aff0-4089-9700-03dc5c965113.

4.1 Optically thick, LTE limit

In this limit, the one-zone line luminosity is

$$L = V \times n_u A \beta_S h\nu = V \frac{n_u A h\nu}{n_l A \lambda^3 \frac{1}{8\pi} \frac{g_u}{g_l} t \left(1 - \frac{g_l}{g_u}\frac{n_u}{n_l}\right)}$$
$$= V \frac{8\pi h\nu}{\lambda^3} t^{-1} \frac{e^{-h\nu/kT}}{\left(1 - e^{-h\nu/kT}\right)} = \frac{4\pi V}{ct} \lambda B_\lambda(T), \quad (3)$$

where V is the volume, n_u and n_l are the number densities of the upper and lower states, A is the Einstein coefficient for spontaneous emission, β_S is the Sobolev escape probability, g_u and g_l are the statistical weights of the upper and lower levels, t is time, and the other symbols have their usual meaning. If $h\nu \ll kT$, then $e^{-h\nu/kT} \approx 1 - h\nu/kT$, giving

$$L \approx \frac{8\pi k}{\lambda^3 t} V T. \quad (4)$$

4.2 Strong NLTE limit

Assuming that collisional excitation from n_l dominates the inflow to n_u, but the electron density n_e is low enough that deexcitation is always radiative, we have

$$n_u A \beta_S = n_l n_e \frac{8.6 \times 10^{-6}}{\sqrt{T}} \frac{1}{g_l} \Upsilon(T) e^{-h\nu/kT}, \quad (5)$$

where Υ is the effective collision strength, usually weakly dependent on temperature. Then

$$L = V \frac{hc}{\lambda} n_l n_e \frac{8.6 \times 10^{-6}}{\sqrt{T}} \frac{1}{g_l} \Upsilon e^{-h\nu/kT}. \quad (6)$$

Taking $n_l \approx n_{ion}$, and using $M_{ion} = V n_{ion} \mu m_p$, where μ is the atomic weight of the ion in a.m.u., this becomes

$$L \approx \frac{8.6 \times 10^{-6} hc}{\lambda g_l \mu m_p} T^{-1/2} e^{-h\nu/kT} M_{\rm ion} n_e \Upsilon. \quad (7)$$

If $h\nu \ll kT$, then the exponential factor approaches unity. Because Υ-factors have weak T-dependencies, the temperature dependency is then approximately $\propto T^{-1/2}$.

4.3 Optically thin, LTE limit

This limit yields

$$L = V n_l \frac{g_u}{g_l} e^{-h\nu/kT} A h\nu = \frac{hc}{\lambda \mu m_p} \frac{g_u}{g_l} e^{-h\nu/kT} M_{\rm ion} A. \quad (8)$$

If $h\nu \ll kT$, then the exponential factor approaches unity, so there is no temperature-dependency.

4.4 Summary

Thus, line formation can occur in three different regimes. For $T \gg T_{exc}$ (often fulfilled for MIR lines), the optically thick LTE regimes probes $V \times T$ (equation 4), the strong NLTE regime

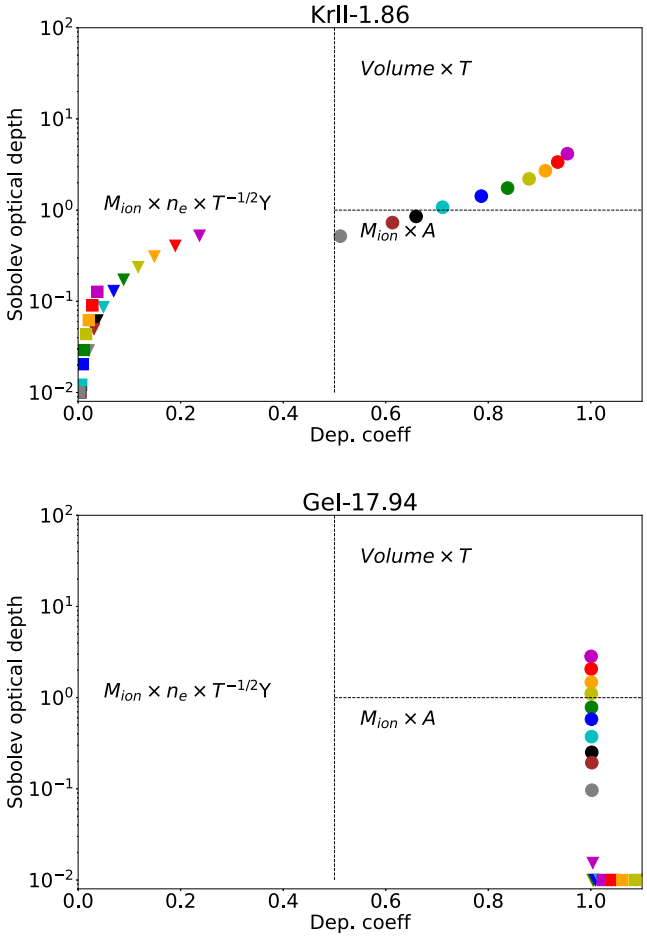

Figure 2. Formation regimes for [Kr II] 1.86 μm (top) and [Ge I] 17.94 μm (bottom), in model A at 10 d (circles), 40 d (triangles), and 80 d (squares). The *x*-axis shows departure coefficient for the upper level, and *y*-axis the Sobolev optical depth for the transition. Each colour corresponds to a zone, with purple the innermost zone. Zone 1 has $v \sim 0.02c$, and zone 10 has $v \sim 0.06c$. The stated temperature-dependencies are for the limit $T \gg T_{exc}$.

probes $M_{ion} \times n_e/\sqrt{T}$ (equation 7), and the optically thin LTE regime probes M_{ion} (equation 8). Even if the luminosity is generated over a region with varying physical conditions, the total luminosity may still robustly reveal information on masses or volumes. For example, if formation is in the third regime, it does not matter how T and n_e vary over the region. If formation is in the first regime, the emission volume can be inferred no matter what the n_e distribution is (and if a good average temperature can be assessed).

Note that while lines with $\lambda < hc/kT$ are more sensitive to temperature than equations (4), (7), and (8) limits, ratios of such lines with similar excitation energies can still give abundances ratios to good accuracy.

Fig. 2 plots the position in the departure coefficient (level population relative to its value for the case of an atom in LTE) – optical depth plane for the [Kr II] 1.86 μm and [Ge I] 17.94 μm lines, in model A, as examples. For each epoch, the values in the innermost 10 zones are plotted, which are the ones with the most energy deposition, and therefore will be dominant for line formation. Dividing lines between the different line formation limits discussed above are also drawn.

[Kr II] 1.86 μm is at 10 d mostly in the upper right corner, which means its luminosity probes volume but not mass. At 40 and 80 d, on the other hand, it has moved to the left-side domain, which means its luminosity probes the product of Kr II mass and electron number density (and $T^{-1/2}$). Thus, by the time the Kr II mass can be diagnosed, the regime is already where there is dependency on n_e– the line never (cleanly) passes through the $M_{\rm ion}A$ regime (bottom right).

[Ge I] 17.94 μm (bottom panel) behaves differently. It straddles the upper-right and bottom-right regimes at 10 d, indicating hybrid formation that needs detailed modelling for interpretation. Then, at 40 and 80 d, the line is fully in the bottom-right corner, which means direct probing of $M_{\rm ion}$. As the departure coefficients are close to unity (LTE), the line is far away from any n_e sensitivity which gives good robustness for mass inferences.

The accuracy to which an ionic mass can be inferred in the most favourable case; optically thin LTE and $T_{exc} \ll T$ depends in theory on the accuracy of the A-value of the transition only. These are known to expected accuracies of a few per cent for the low-lying M1/E2 transitions giving the dominant IR lines. In practice, the accuracy will be more limited by uncertainty in the exact value of $\exp(-T_{\rm exc}/T)$, which e.g. is 0.9 if $T_{\rm exc}/T = 0.1$ but 0.74 if $T_{\rm exc}/T = 0.3$. Uncertainty in the measured line luminosity, coming from uncertainties in distance, flux calibration, and blending with other lines, will in many cases also be influential for which accuracy masses can be determined to.

By studying the spatial and temporal variation of these formation regimes, it is possible to identify which lines give what diagnostic information at which epochs – valuable for developing high-return observation strategies.

5 RESULTS

5.1 Model A, evolution of physical conditions

Over the modelled time span (10–80 d), model A has a radioactive powering (after thermalization) ranging from 4.6×10^{39} erg s^{-1} at 10 d to 9.1×10^{38} erg s^{-1} at 80 d, which is a factor 5.1 decline. This is a significantly smaller power decline than a canonical $t^{-1.3}$ decay (and declining thermalization efficiency would steepen further) which would give a factor $\gtrsim$15. The reason is that at this Y_e a few isotopes dominate the power output rather than a large ensemble. The power for $Y_e \sim 0.35$ is lower than for low-Y_e compositions at 10d (by a factor 3–4), but higher at 80 d (by a factor ∼2; S. Wanajo et al. 2014).

Fig. 3 (top) shows the cumulative radioactive deposition versus velocity in model A. Some $\gtrsim$80 per cent of the deposition occurs in the layers inside $0.07c$, corresponding to the inner ∼10 shells of the total 25. The central region dominance can be seen to increase with time, as thermalization inefficiency increasingly sets in for the outer layers. This effect will lead to a narrowing of emission lines with time, and hence cleaner, less blended spectra at late nebular epochs.

Fig. 3 (middle) shows the temperature versus velocity at the three epochs. At 10 d, the ejecta are close to isothermal at around 2300 K in the line-forming region ($v/c \lesssim 0.07$). With time there is then a general trend of increasing temperatures, as radioactive powering decreases more slowly than the collisional cooling efficiency (K. Hotokezaka et al. 2021; Q. Pognan et al. 2022a), although the innermost few zones break this trend and become somewhat cooler between 10 and 40 d (changes in ionization and reduced photon trapping can also affect the temperature). In

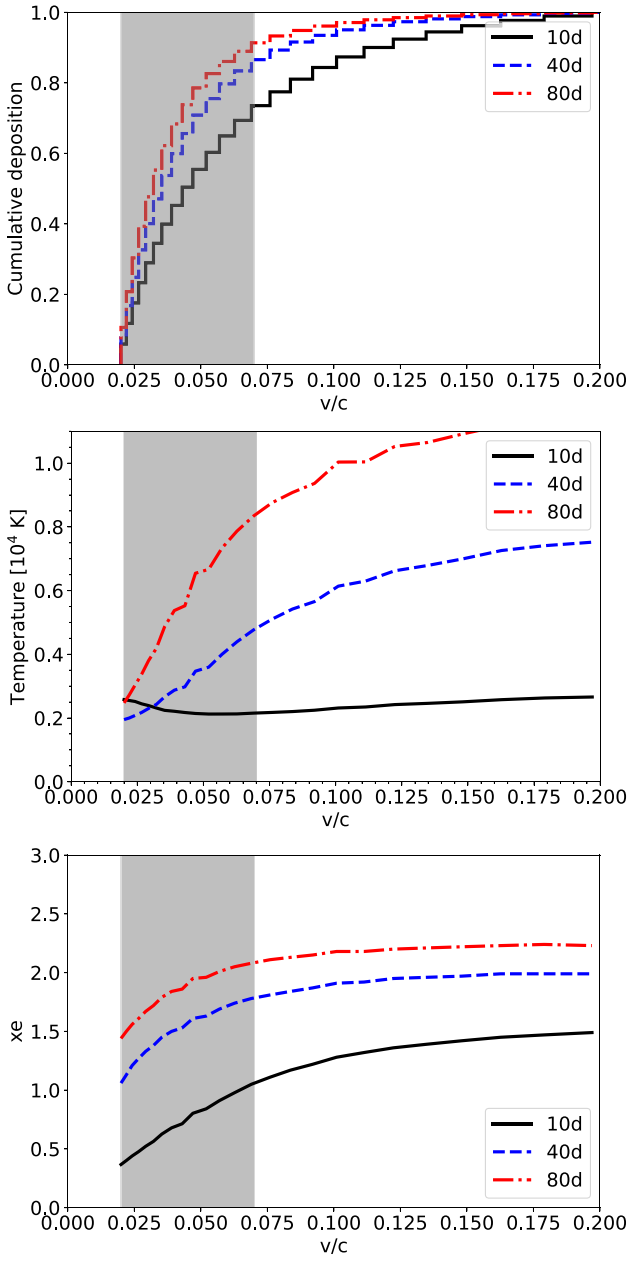

Figure 3. Physical conditions in model A; cumulative radioactive deposition (top), electron temperature (middle), electron fraction (bottom), at 10 d (black, solid), 40 d (blue, dashed), and 80 d (red, dash–dotted). The $\gtrsim$80 per cent deposition region is marked grey.

contrast to at 10 d, there is at later epochs a quite steep temperature gradient ($\sim 2000 - 5000$ K over $v/c = 0.02 - 0.07$ at 40 d and $\sim 2500 - 8000$ K at 80 d). The general temperature scale in the line-forming region indicates that emission lines with $\lambda \gtrsim hc/(k \times 2000\,\mathrm{K}) \gtrsim 7$ μm will at all epochs be quite insensitive to the detailed temperature (proportional to T^α, where $\alpha = -1/2, 0, 1$, depending on regime, as opposed to exponential dependency if $\lambda < hc/kT$), making MIR lines uniquely powerful probes.

Fig. 3 (bottom) shows the ionization (electron fraction x_e) versus velocity. In the line-forming region ($\lesssim 0.07c$), the characteristic value is $x_e \sim 0.7$ at 10 d (neutrals and singly ionized species dominate), increasing to $x_e \sim 1.5$ at 40 d (singly and doubly ionized species dominate) and $x_e \sim 1.8$ at 80 d (doubly ionized species dominate). While x_e does increase with velocity coordinate, this effect only slightly dampens the electron density profile from the model density profile ($n_{\mathrm{nuclei}} \propto v^{-3}$), roughly to a $n_e \propto v^{-2}$ form in the inner layers. As such, the electron density varies by about an order of magnitude over the line-forming region ($\sim 0.02 - 0.07\,c$). The variation of T and n_e is important information for assessing single-zone approaches. Ionization structures of selected elements are plotted in Figs C1–C3.

Fig. 4 shows the escape probability for a photon emitted at the centre of the nebula versus wavelength. At 10 d, the optical range is completely opaque, and much of the NIR as well, although certain escape windows exist there, where the line opacity is sufficiently low. The MIR range is optically thin for the most part at 10 d although some lines remain optically thick, causing absorption ranges. By 40 d, the NIR range has largely opened up, and at 80 d conditions are mostly optically thin down to ∼5000 Å, although a few lines remain optically thick in the innermost zones, e.g. Rb I 7802, 7949 Å.

5.2 Spectrum of model A, 10 d

Fig. 5 shows the model spectrum at 1 0d. Line emission is dominated by [Kr II] 1.86 μm, [Br I] 2.71 μm, [Br II] 3.19 μm, [Se I] 5.03 μm, [Ge II] 5.66 μm, [Ge I] 11.72 μm, [Ge I] 17.94 μm , [As II] 9.40 μm, and [Se I] 18.35 μm. There is also some emission in the allowed Sr I transitions between 5s4d(^{3}D) to 5s5p(^{3}P^o) at 2.60–3.01 μm. Emission is also seen for [Ni III] 7.35 μm and [Zr III] 14.67 μm (some blending with [Br II] 14.26 μm).

Fig. 6 (upper left) shows the zone-averaged formation regimes of the main lines at 10 d. We can see that LTE is a quite good approximation, with all departure coefficients $\gtrsim 0.7$. We can also see that many of the lines are still optically thick. In those cases the specific ion masses are not important; each line samples a blackbody (at characteristic line-forming region temperature of ∼2300 K) and only emission volume and temperature affect the line flux (equation 3).

At 2300 K, a blackbody peaks at $hc/(4.96kT) = 1.3$ μm. The closest optically thick LTE line to this is [Kr II] 1.86 μm, which therefore becomes the strongest line in the spectrum. Other optically thick lines then follow on the blackbody curve with peak luminosities in rough agreement with the theoretical limit (optically thick LTE case). Some variation occurs as the volume over which a given transition is optically thick and in LTE can vary. Radiative transfer effects still operate for $\lambda \lesssim 2$ μm (Fig. 4) which there complicates this simple picture.

Comparison to AT2017gfo at + 10.4 d shows that AT2017gfo was brighter by a factor several in the NIR compared to the model. As described above, the $Y_e \approx 0.35$ composition has significantly less decay power than lower-Y_e compositions at this epoch, and the discrepancy is possibly explained by the presence of such low-Y_e material.

Looking at spectral details, the model gives distinct emission lines in the NIR from Zr I 1.37 μm (this may be [Rb III] 1.36 μm emission scattering in optically thick Zr I lines), and [Kr II] 1.86 μm. These lines unfortunately lie in regions of strong atmospheric absorption, and hence the reconstructed flux of E. Pian et al. (2017) is uncertain at these wavelengths. If one takes the reconstructed fluxes at face value, the lack of these features in the observations around 10 d might be due to several reasons. One is opacity provided by heavier elements ($Z > 40$ elements are not included in the model, except Te); Fig. 4 shows that even this

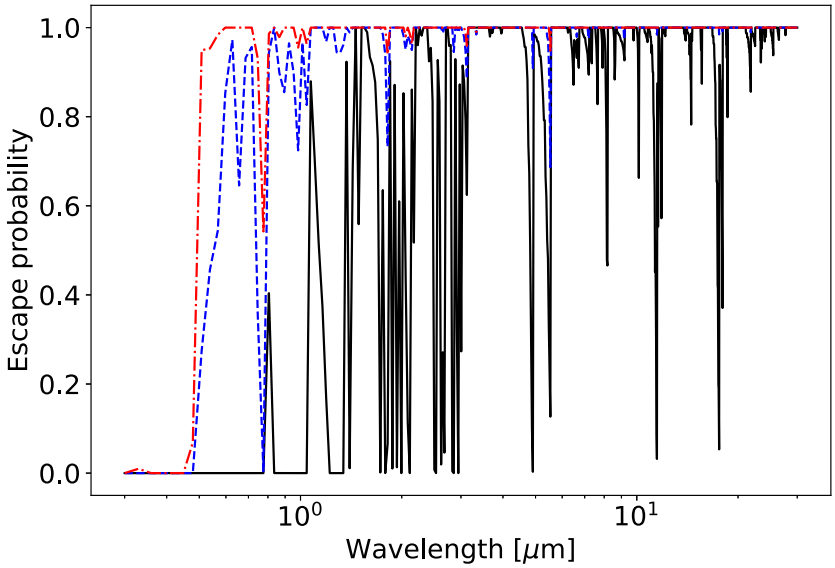

Figure 4. Escape probability for a photon emitted at the centre of the nebula at the modelled epochs (10 d; black, solid, 40 d; blue, dashed, and 80 d; red, dash–dotted) for model A.

light composition is largely optically thick in the NIR at 10 d, and heavier elements would further enhance the opacity. Another is cooling by heavier elements (this would require these elements to be cospatial). Another is that AT2017gfo has significantly less $Z = 30 - 40$ elements than in this model (solar). A final possibility is that the velocity distribution in this model is unrepresentative. However, definitive conclusions cannot be drawn from the ground-based spectra of AT2017gfo. *JWST* observations of KNe, such as those for AT2023vfi (A. J. Levan et al. 2024), are needed to accurately measure the strengths of these Zr I/[Rb III], and [Kr II] features.

Irrespective of which, or combination of which factors, one valuable conclusion is that none of these $Z = 31 - 40$ elements provide a compelling candidate line to explain the strong observed 2.1 μm feature. [Kr III] 2.20 μm would be the line closest in wavelength, but it is relatively weak in the model, with most Kr being in the I and II states. There is also a Zr I line at 2.24 μm (0.02c separation) that is optically thick out to ∼0.05c, absorbing some of the [Kr III] 2.20 μm emission. The tellurium feature is a blend of [Te I] 2.10 μm and [Te III] 2.10 μm in this model. Its luminosity is substantially below the observed value. The Te I lines becomes stronger than the Te III line when ionization is low/moderate, and can give signatures also in core-collapse SN models (G. Ricigliano, K. Hotokezaka & A. Arcones 2025).

5.2.1 Kr discussion. [Kr III] 2.20 μm is one of only three lines (the others being [Te III] 2.10 μm and [Br II] 3.19 μm) that directly probe ion mass at this epoch (Fig. 6). It is however quite weak, as only about 1 per cent of the Kr in the model is in the III state. Dividing equation (8) with equation (3), and using $A = 2.0\ \mathrm{s}^{-1}$, $M_{\mathrm{Kr\,III}} = 10^{-4}\ \mathrm{M}_\odot$, $v = 0.05c$, gives $L_{\mathrm{LTE,thin}}/L_{\mathrm{LTE,thick}} \sim 0.1$.

Let us consider ways to bring the [Kr III] line up towards observed levels for the 2.1 μm feature. If a different ionization structure would increase the Kr III abundance by a factor 10, the line would move into the optically thick regime, for the same overall density, and line luminosity would go up by a factor ∼10, all else remaining similar, according to the above ratio. Changing the volume would not easily achieve this, as a smaller volume would reduce the LTE, optically thick regime luminosity, and a larger volume would not achieve optical thickness (and would also move the regime towards NLTE). Increasing power would be more promising. It would lead to more Kr III, and a higher temperature. But, as long as a significant Kr II abundance exists, [Kr II] 1.86 μm would also strengthen. It would seem difficult to achieve a strong [Kr III] line but a weak [Kr II] line (with the caveat that most of the [Kr II] spectral feature lies is blocked by atmospheric absorption), unless the doubly ionized state becomes dominant to the singly ionized state; in the model the opposite relation holds, and calculated recombination rates for the Kr ions are in use (even though dielectronic recombination (DR) calculations for the quite low temperatures here carry uncertainties, e.g. G. J. Ferland 2003; N. C. Sterling et al. 2015).

5.3 Spectrum of model A, 40 d

The spectrum at 40 d is shown in Fig. 7. The neutral germanium lines have now significantly weakened, as ionization has increased. The iron-group elements give relatively strong emission between $10 - 13$ μm, and also by [Ni II] 7.35 μm, whereas [Br II] and [Zr III] create a blend at around 14 μm. Clear detection potential is predicted for Ni, As, Br, Kr, Se, and Ge.

All strong lines are now optically thin (Fig. 6). The long-wavelength lines are still close to LTE, whereas the shorter-wavelength ones are now in the NLTE regime – it is however still the same lines that dominate as at 10 d. The somewhat higher ionization leads to the [Kr III]/[Kr II], [Br II]/[Br I], and [Ge II]/[Ge I] line ratios now being higher.

The model predicts the best targets for direct ion mass determinations (optically thin, close to LTE, and weak T sensitivity) to be [Ge I] 17.94 μm, [Ge I] 11.72 μm, [Ge II] 5.66 μm, and [Se I] 5.03 μm. The Ge I lines are however quite weak and blended, but the [Ge II] and [Se I] lines are strong. Neutral Ge makes up 1–10 per cent of the Ge in the line-forming region, and singly ionized Ge $\gtrsim$60 per cent. Therefore joint observations of the Ge I and Ge II emission lines holds promise to get a good constraint on the total Ge mass. Selenium has a substantial Se II

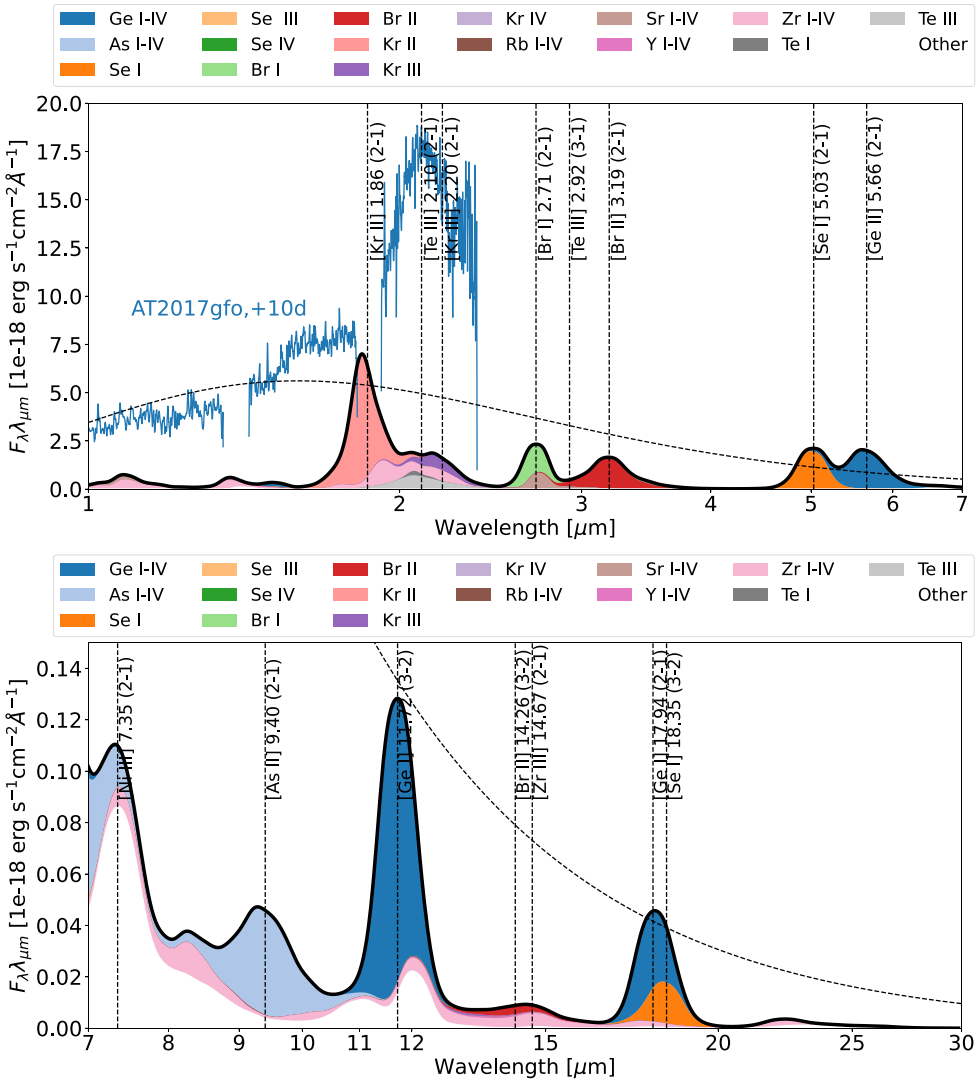

Figure 5. Spectrum of model A at 10 d. The observed (ground-based) spectrum of AT2017gfo at + 10.4 d (E. Pian et al. 2017) is plotted in blue. Overplotted is also a 2300 K blackbody (black, dashed) – lines forming in the optically thick LTE regime have peak fluxes at or close to this curve.

abundance ($\gtrsim$ 50 per cent), which means observations of the I and III lines (Se II gives no strong lines) still need a significant correction factor to estimate the total Se mass.

The strongest line in the model is, as at 10 d, [Kr II] 1.86 μm. There is no sign of this line in the + 29 d *JWST* spectrum of AT2023vfi. At this epoch, there is also no possibility to shift model flux over to the [Kr III] 2.20 μm line (by a higher ionization state); it is already too strong in the model compared to observations. While at 10 d radiative transfer effects at these wavelengths are still present to some degree, at 40 d they are minor (at least from the elements included here, and models including also heavier elements show little absorption by these, Q. Pognan et al. 2026); the model predicts none that could absorb [Kr II] 1.86 μm or [Kr III] 2.20 μm emission.

It would seem difficult to resolve this 'Kr issue' with either an ionization effect (only small fractions reside in I and IV states) or a radiative transfer effect (epoch is too late). Apart from the option of there being little or no Kr in the ejecta, the remaining option is a lower temperature. If the temperature were 1500 K instead of the roughly 3000 K in the model, the [Kr II] 1.86 μm luminosity would go down a factor 9. This might happen if there are many other cooling lines from heavier elements, not included in the model, as observations of AT2023vfi may suggest with its smooth spectrum. A counterpoint to this is that the power in model A is quite low, clearly lower than what is needed for AT2017gfo at + 10 d (by a factor ∼5) and for AT2023vfi at + 29 d (factor ∼2) – but heavier elements will bring in higher power, acting to raise the temperature.

The Te emission is at this epoch almost exclusively due to [Te III] 2.10 μm. The luminosity is, as at 10 d, similar to the [Kr II] + [Kr III] emission. The observed feature in AT2023vfi has a peak close to 2 μm, not in clean agreement with any line.

5.4 Spectrum of model A, 80 d

The spectrum at 80 d is shown in Fig. 8. The ejecta are now somewhat hotter (characteristic temperature in the line-forming region of ∼5000 K) and more ionized (characteristic x_e of ∼1.8),

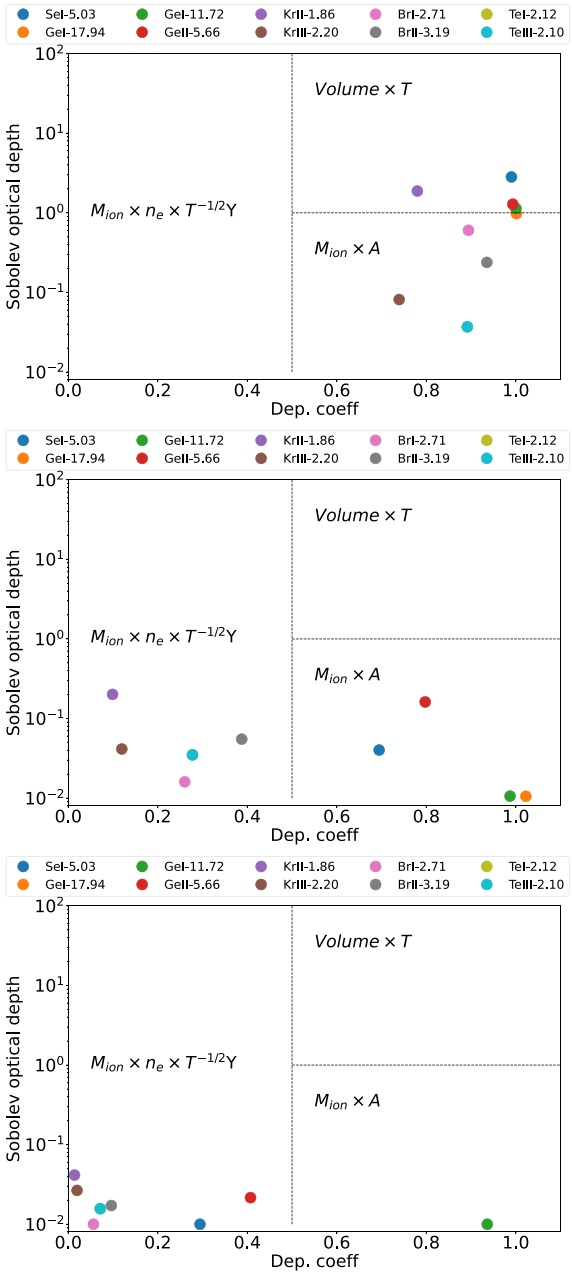

Figure 6. Formation regimes in model A at 10 d (top), 40 d (middle), and 80 d (bottom). Each point represents the zone-averaged value over the innermost eight shells. Optical depths below 10^{-2} are plotted at this floor value. The stated temperature dependencies are for the limit $T \gg T_{\rm exc}$.

than at 40 d. The $1-10$ μm region is qualitatively similar as at $+$ 40 d, although the line luminosities are down by a factor ∼2. The neutral lines have now mostly disappeared. In the $10-30$ μm range, the Ge I lines have disappeared, while some of the other features remain at similar luminosities as at 40 d. The iron-group cluster at $10-13$ μm has strengthened further, and it blends into a complex of lines from Ge I, Zr III, Kr III, and Br II extending up to 15 μm.

The $+$ 74 d *Spitzer* 4.5 μm observation of AT2017gfo is matched reasonably well by the combination of [Se III] 4.55 μm and [Se I] 5.03 μm emission in the model. As at 40 d, the 3.6 μm upper limit is at or somewhat below the model prediction – with [Br II] 3.19 μm tending to give a bit too much luminosity into the band.

For AT2023vfi, the predicted [Br II] 3.19 μm line is not, as at 40 d, observed, and the issue with [Kr II] 1.86 μm is also still there. The observed feature seen close to 2.1 μm lies somewhat more towards the red at $+$ 61 d, and would match with a relatively flat-topped [Kr III] 2.20 μm line – in model A the line is however too narrow. Both the [Kr III] 2.20 μm and [Te III] 2.10 μm model lines have similar luminosities as the AT2023vfi feature.

5.5 Model B – evolution of physical conditions

The physical conditions in model B are plotted in Fig. 9. Model B reaches 80 per cent deposition at $v/c \sim 0.15$, thus emission lines will emerge a factor 2–3 broader than in model A. In terms of power levels, the factor ∼3 decay boost combines with lower thermalization efficiencies (due to the lower densities) to give deposition ratios, relative to model A, of 2.2, 1.3 and 0.9 at 10, 40, and 80 d, respectively.

The lower densities, and the higher deposition (except at 80 d), lead to higher temperatures, especially at 40 and 80 d when model B reaches characteristic temperatures of 10 000 and 20 000 K, much higher than model A (∼3000 and ∼6000 K, respectively). This means that more IR lines now come into the regime $T_{\rm exc} \ll T$. Ionization is also higher, with x_e values up by factors ∼ 1.5.

Ionization structures of selected elements are plotted in Figs C4–C6. At 40 and 80 d in this model, the triply-ionized state is the dominant ion for some elements. If the 4-times ionized state is significantly populated, this can lead to an artificially large abundance in the IV charge state in our models, which do not include higher ionization states. This is likely to be the case when the fraction of the IV state exceeds ∼2/3, as is the case for Ge, As, Kr, and Zr. Of these species, only [Zr IV] has a detectable line (at 8.00 μm) in the wavelength range considered, and thus the flux of this line in Figs 12 and 13 should be considered an upper limit. No such effect is found in model A at any epoch.

We also looked at possible IR lines from (not included) V stages; neither Ge V, As V, Se V, Rb V, Sr V, Y V, Zr V, or Te V have any potential strong IR lines. Ga V has its 2–1 (fine-structure) line at 2.79 μm, Kr V has its 2–1 transition at 2.67 μm, and 3–2 at 1.36 μm. Br V has its 2–1 transition at 1.64 μm.

5.6 Spectrum of model B – 10 d

The spectrum of model B at 10 d is shown in Fig. 10. [Kr II] 1.86 μm is, as in model A, the strongest line. [Kr III] 2.20 μm is significantly stronger than in model A, which together with the [Te III] 2.10 μm contribution moves the blend towards the red, giving a peak at ∼2 μm. The Kr lines are now formally consistent with the AT2017gfo spectrum, but the shape of the triple-blend feature is also not in particularly good agreement with the observed feature, which is quite well described by a Gaussian centred at 2.1 μm (which would correspond to a Gaussian emissivity distribution if by a single line, A. Jerkstrand 2017). Considering the 7.4–10.4 d evolution, J. H. Gillanders et al. (2024) favour a fit consisting of two Gaussians centred at 2.05 and 2.14 μm, respectively, with $v_{\rm FWHM} = 0.1c$. It is of interest that these wavelengths would match [Te III] 2.10 μm and [Kr III] 2.20 μm if both have a blueshift of $\sim 0.05/2.1 = 0.024c$. Such a blueshift could arise either due to an intrinsic ejecta asymmetry, or due to radiative transfer effects (A. Jerkstrand et al. 2015).

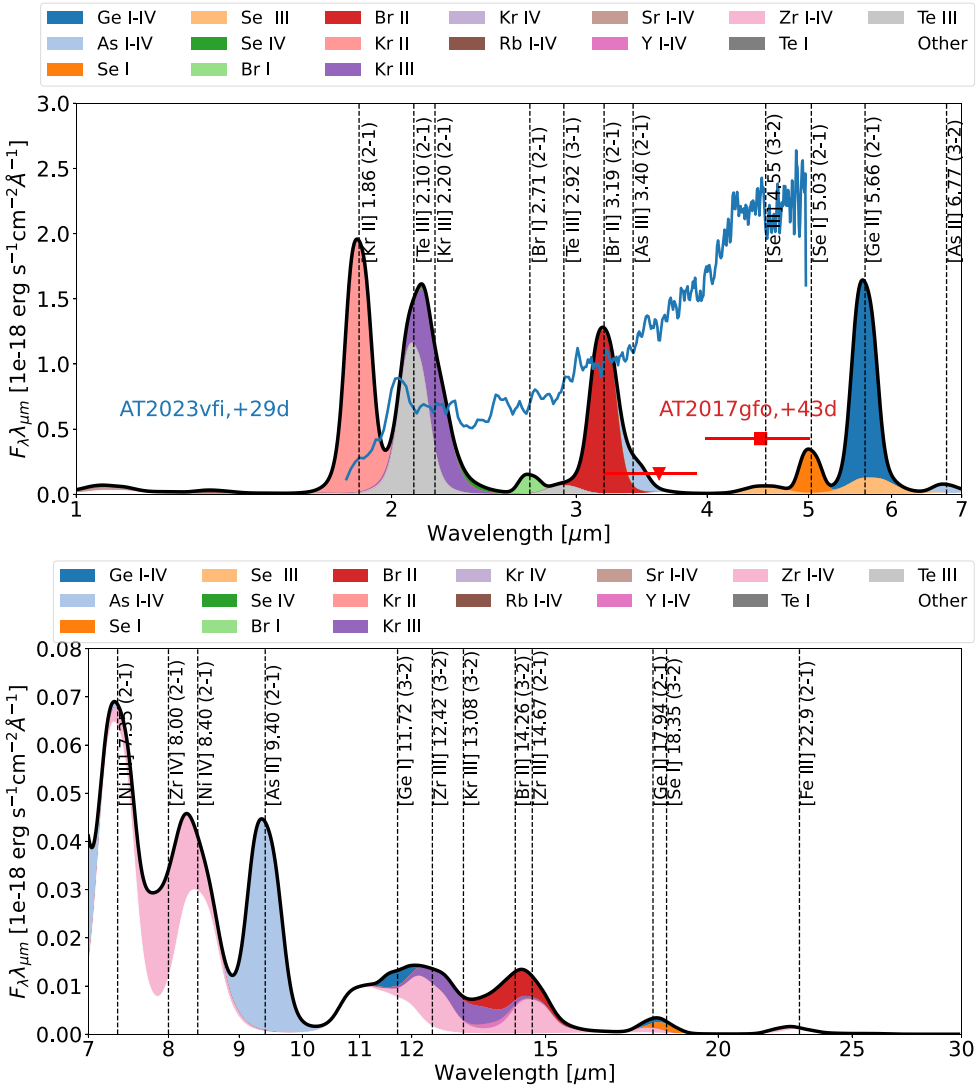

Figure 7. Spectrum of model A at 40 d. Observed photometry of AT2017gfo at +43 d and observed spectra of AT2023vfi at + 29 d are also shown. The model and AT2023vfi spectra have been scaled to a distance of 40 Mpc (distance of AT2017gfo).

At longer wavelengths, [Br II] 3.19 μm and [Ge II] 5.66 μm are distinct, as in model A. The neutral lines, [Br I] 2.71 μm and [Se I] 5.03 μm are now however mostly gone, as is the NIR contribution by zirconium (much of it is Zr I in model A, and neutral abundances are generally lower in model B).

Beyond 10 μm, the neutral Ge lines in model A are gone, and instead [Kr III] 13.08 μm and [Br II] 14.26 μm have emerged – the flux levels are however low and there is severe blending throughout. This model predicts observations between 1–7 μm to be most rewarding (in terms of lines least affected by blending), and Br II and Ge II appear promising for detection at ∼10 d irrespective of the velocity of the light *r*-process component (strong lines predicted by both models A and B). Inspection of the line formation regimes (Fig. 11) shows that Br II and Ge II form in the optically thin LTE regime, thus with this type of ejecta the ionic masses are possible to directly probe at 10 d. The fractions of Br and Ge in the singly ionized states are quite high in the model (20–50 per cent for Br and ∼80 per cent for Ge, Fig. C4), so these ionic masses are in turn useful tracers of the total element masses.

5.7 Spectrum of model B – 40 d

The spectrum of model B at 40 d is shown in Fig. 12. The narrow [Kr II] 1.86 μm line in model A has here morphed into a broader feature. The [Kr II] 1.86 μm luminosity is now subdominant to [Kr III] 2.20 μm and in addition [Se IV] 2.29 μm has emerged, with even more luminosity than the [Kr III] line. Together with a relatively modest [Te III] 2.10 μm contribution, the 2.1 feature is therefore now a four-way blend. The model feature is in reasonably good agreement with the observed feature in AT2023vfi, both in terms of luminosity and (roughly) line profile – although the detailed interpretation depends on what one assumes about the underlying (quasi)-continuum.

Neutral Br and Ge lines are weak, while [Br II] 3.19 μm is present, with some blending of [As III] 3.40 μm. Both [Se I] 5.03 μm and [Ge II] 5.66 μm have disappeared and given way to [Se III] 4.55 μm and [Se III] 5.74 μm. What one may note is that in both a low- and high-velocity model, it is always selenium that would produce the type of flux observed with *Spitzer* for AT2017gfo – neutral selenium in the first case and doubly ionized selenium

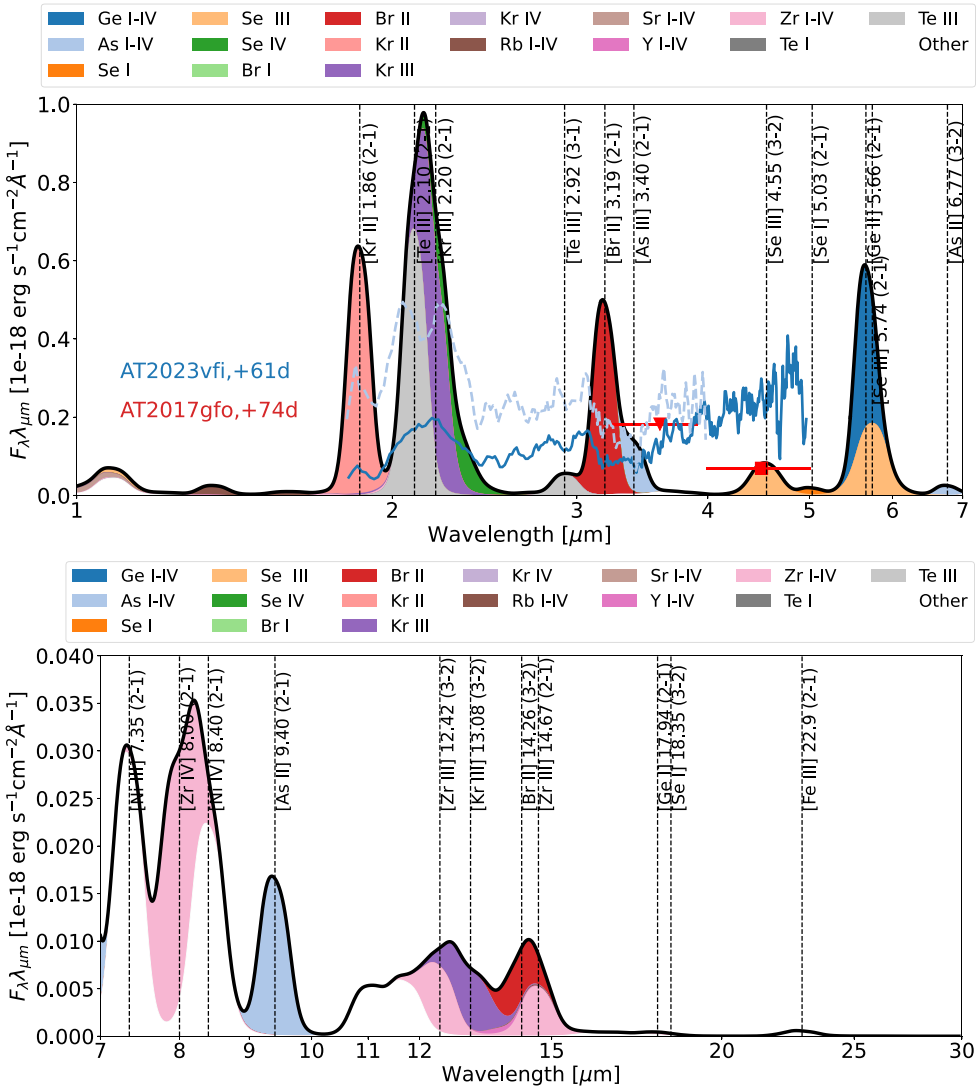

Figure 8. Spectrum of model A at 80 d. Observed photometry of AT2017gfo at +74 d and observed spectra of AT2023vfi at + 61 d are also shown; our standard reduction set (J. H. Gillanders & S. J. Smartt 2025) is plotted solid, we plot also the reduction of A. J. Levan et al. (2024, dashed) for completeness. The model and AT2023vfi spectra have been scaled to a distance of 40 Mpc (distance of AT2017gfo).

in the second case. At longer wavelengths, [Zr IV] 8.00 μm and [Kr III] 13.08 μm are the dominant lines.

All lines are now well into the low-density limit ('strong NLTE') in the line formation plane (Fig. 11) – thus A-values play no role for the line luminosities, which instead are directly proportional to collision strengths. In addition, as the temperature is $\gtrsim$ 10 000 K, relative IR line luminosities are temperature insensitive and differ mainly by the combination of ionic masses and collision strengths. The models make use of detailed collision strengths for the Kr II, Kr III, Se III, Se IV, Te III, and Zr IV transitions but not for Br II lines.

5.8 Spectrum of model B – 80 d

The spectrum of model B at 80 d is shown in Fig. 13. Changes to + 40 d are quantitative but not qualitative. [Se IV] 2.29 μm now contributes the majority of the flux in the 2.1 μm blend, with [Kr III] 2.20 μm having second strongest contribution. As at 40 d, a solar ratio between Te and the lighter elements would mean Te does not dominate the feature. The [Se III] 4.55 μm line remains in reasonable agreement with the *Spitzer* observations – spectral observations with *JWST* of the 5–7 μm region hold potential to confirm or reject Se III based on the 5.74 μm line.

Evolution beyond 10 μm is minor – the same lines are seen as at 40 d and they are formed in the same regime, the model therefore predicts limited additional value of observing at the long wavelengths again if data at ∼40 d already exists.

5.9 Summary of predicted signatures

Table 2 summarizes predicted signatures from the $Z = 31 - 40$ elements in the two models. Six of these 10 elements are predicted to have detectable lines; Ge, As, Se, Br, Kr, and Zr. The other four elements – Ga, Rb, Sr, and Y – give no strong IR lines in the models, at any epoch.

This table can be used to design a *JWST* observation strategy depending on target element. For example, detection of Ge is predicted to require one MIRI spectrum at around 10 d – (unblended)

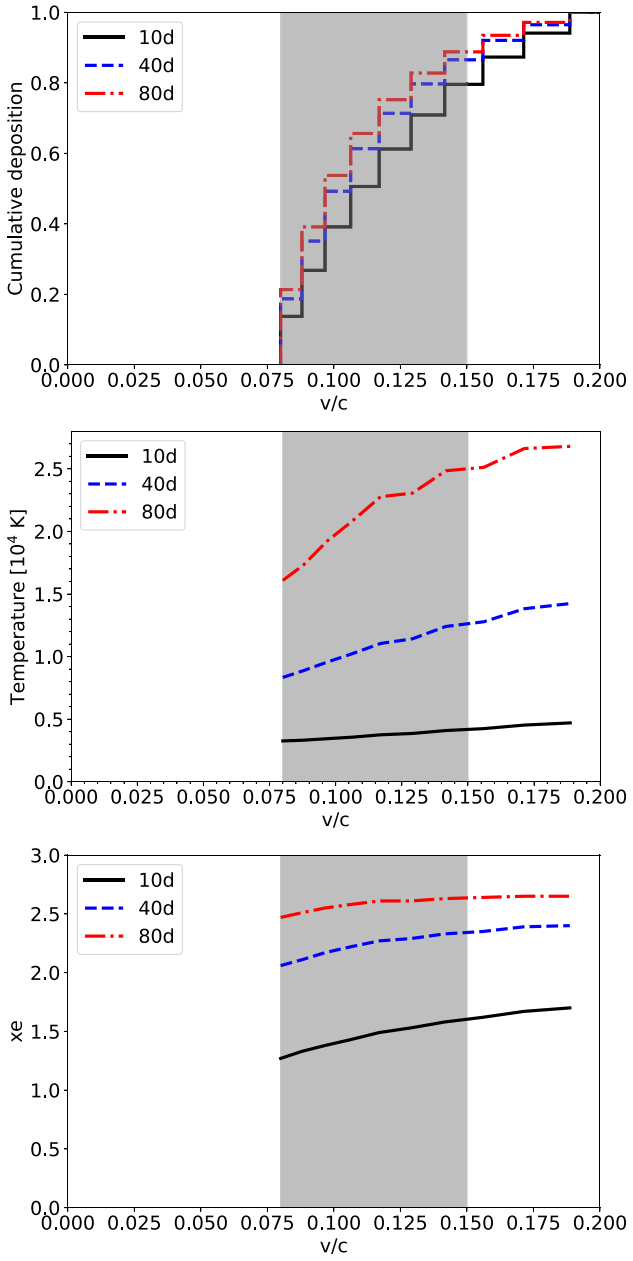

Figure 9. Physical conditions in model B; cumulative radioactive deposition (top), electron temperature (middle), electron fraction (bottom), at 10 d (black, solid), 40 d (blue, dashed), and 80 d (red, dash–dotted). The $\gtrsim$80 per cent deposition region is marked grey.

Ge I lines should emerge if ejecta conditions are similar to model A, and Ge II lines if they are similar to conditions in model B. Analogously, a NIRSpec spectrum at 10–40 d holds potential to reveal Br I and Br II for model A conditions and Br II (and perhaps Br IV) for model B conditions.

6 DISCUSSION

From the considered model set, krypton stands out as an element giving strong predicted lines that are not clearly seen in the observations of AT2017gfo and AT2023vfi. We therefore look in some detail into the formation of these lines, and what constraints may be put on krypton abundances.

In the optically thin LTE limit, the line ratio of [Kr III] 2.20 μm and [Te III] 2.10 is given by

$$\frac{L(\mathrm{Kr\,III})}{L(\mathrm{Te\,III})} = \frac{x_{\mathrm{Kr}}}{x_{\mathrm{Te}}}\frac{y_{\mathrm{Kr},3}}{y_{\mathrm{Te},3}}\frac{g_{\mathrm{u,Kr\,III}}/Z_{\mathrm{Kr\,III}}(T)}{g_{\mathrm{u,Te\,III}}/Z_{\mathrm{Te\,III}}(T)}\frac{\mathrm{A}_{\mathrm{Kr\,III}}}{\mathrm{A}_{\mathrm{Te\,III}}}\frac{h\nu_{\mathrm{Kr\,III}}}{h\nu_{\mathrm{Te\,III}}}e^{\frac{302\,\mathrm{K}}{T}} \approx 3.5\frac{y_{\mathrm{Kr},3}}{y_{\mathrm{Te},3}}. \quad (9)$$

where x_{El} denotes the number fraction of the element and $y_{El,n}$ denotes the fraction of that element in ionization state n, with $n = 1$ representing the neutral atom. The last equation uses the solar (r-process component) value of $x_{\mathrm{Kr}}/x_{\mathrm{Te}} = 8.7$, and, because the temperature is much higher than 302 K, the last term has been put to unity. It also takes the partition function ratio to be $Z_{\mathrm{Kr\,III}}/Z_{\mathrm{Te\,III}} \approx 4$ (it varies between 2–5 over $T = 0 - 10\,000$ K).

Past some time ($\gtrsim$40 d in model B), the lines both form in the low-density NLTE regime. Their luminosity ratio is then, approximating most of the ions to be in their ground states,

$$\frac{L(\mathrm{Kr\,III})}{L(\mathrm{Te\,III})} = \frac{x_{\mathrm{Kr}}}{x_{\mathrm{Te}}}\frac{y_{\mathrm{Kr},3}}{y_{\mathrm{Te},3}}\frac{\Upsilon_{\mathrm{Kr\,III}}/g_{\mathrm{u,Kr\,III}}}{\Upsilon_{\mathrm{Te\,III}}/g_{\mathrm{u,Te\,III}}}\frac{h\nu_{\mathrm{Kr\,III}}}{h\nu_{\mathrm{Te\,III}}}e^{\frac{302\,\mathrm{K}}{T}}, \quad (10)$$

Inserting the known values of the collision strengths (T. Schöning 1997; S. Madonna et al. 2018), and again putting the temperature factor to unity, this becomes

$$\frac{L(\mathrm{Kr\,III})}{L(\mathrm{Te\,III})} \approx 4.9\frac{y_{\mathrm{Kr},3}}{y_{\mathrm{Te},3}}. \quad (11)$$

Thus, for a solar Kr/Te ratio the Te III line can dominate the Kr III one only if the fraction of Te in the doubly ionized state is at least a factor $3 - 5$ larger than the fraction of Kr in the doubly ionized state.

Kr I and Kr II have higher ionization potentials (14.0 and 24.4 eV, respectively) than Te I and Te II (9.0 and 18.6 eV, respectively). All else equal, this would imply that more Kr stays in neutral and singly ionized states compared to Te. However, recombination rates also affect this. For Kr we use calculated rates (N. C. Sterling 2011), so there is limited uncertainty from this direction (although DR calculations are challenging due to uncertain positions of doubly excited states). While for Te only the Te III to Te II recombination stage has published rates (S. Singh, Z. Harman & C. H. Keitel 2025), this does not directly affect the question of how to achieve a lower $y_{\mathrm{Kr},3}/y_{\mathrm{Te},3}$ ratio (to allow Te III to be responsible for the 2.1 μm feature at a solar Kr/Te ratio), as in the models here $y_{\mathrm{Te},3}$ is already large, $\gtrsim 0.3$.

In model A, the characteristic $y_{\mathrm{Kr},3}$ value in the line-forming region is ∼1 per cent at 10 d, growing to ∼10 per cent at 40 d and ∼30 per cent at 80 d (Figs C1–C3). The corresponding $y_{\mathrm{Te},3}$ values are ∼5 per cent, 50 per cent, and 70 per cent. Thus, at 40 and 80 d, the $y_{\mathrm{Te},3}$ value is close to its maximum (unity), and to make a significantly weaker [Kr III] contribution would mean reducing $y_{\mathrm{Kr},3}$. But $y_{\mathrm{Kr},2}$ is already high, and would, for a movement toward a less ionized solution, become yet higher, further overproducing the [Kr II] 1.86 μm line.

In model B, both $y_{\mathrm{Kr},3}$ and $y_{\mathrm{Te},3}$ are high at all epochs, $\gtrsim$ 40 per cent (Figs C4–C6). At 40 and 80 d, the neutral and singly ionized states are subdominant and Kr and Te are mainly in the doubly and triply ionized states. But again, because the krypton recombination rates are known, it is not straightforward to reduce the $y_{\mathrm{Kr},3}$ value.

An analogous analysis of [Kr II] 1.86 μm gives, in the optically thin LTE phase, using $Z_{\mathrm{Kr\,II}}/Z_{\mathrm{Te\,III}} \approx 2$ (range $1 - 4$ over

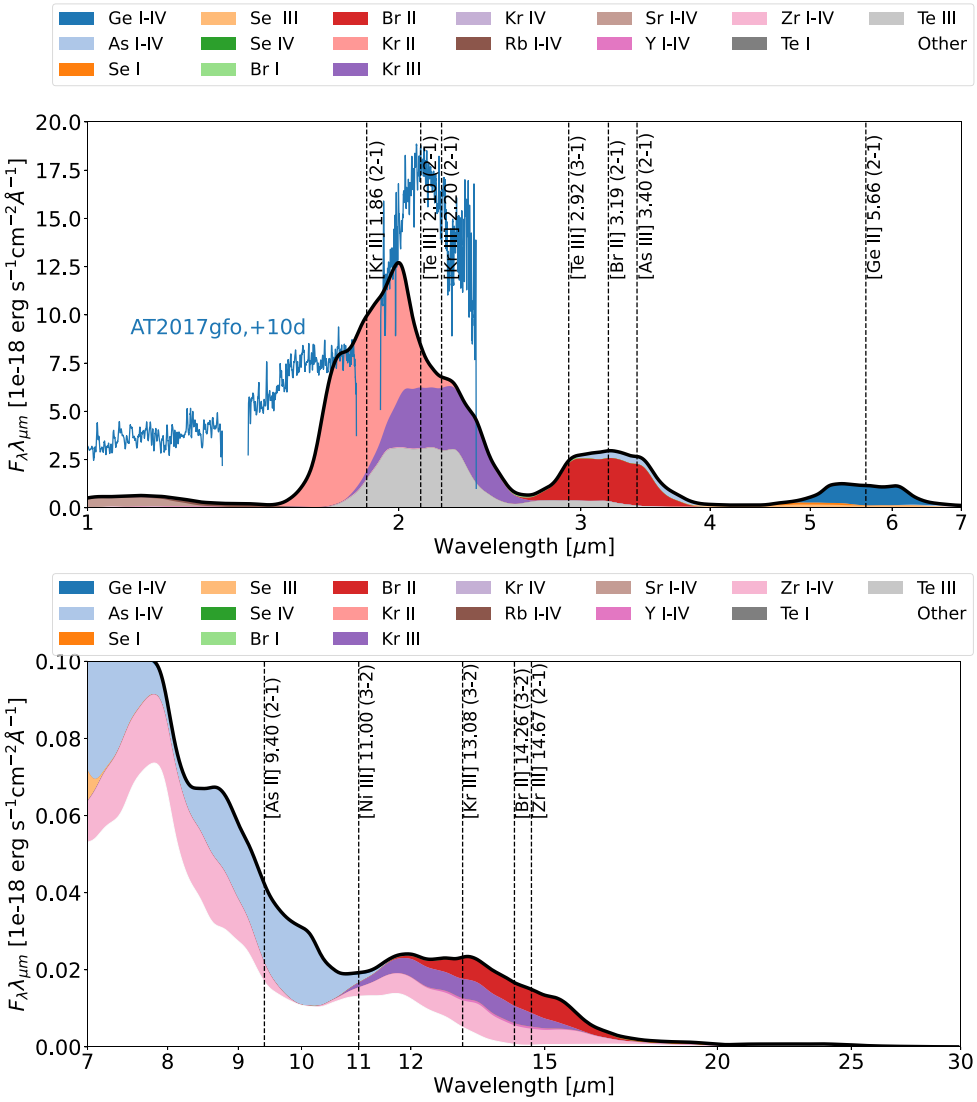

Figure 10. Spectrum of model B at 10 d, compared to the same data as in Fig. 5.

$0 - 10\,000$ K),

$$\frac{L(\mathrm{Kr\,II})}{L(\mathrm{Te\,III})} \approx 7.6 \frac{y_{\mathrm{Kr},2}}{y_{\mathrm{Te},3}} e^{\frac{-884\ \mathrm{K}}{T}}, \tag{12}$$

and in the low-density limit

$$\frac{L(\mathrm{Kr\,II})}{L(\mathrm{Te\,III})} \approx 8.1 \frac{y_{\mathrm{Kr},2}}{y_{\mathrm{Te},3}} e^{\frac{-884\ \mathrm{K}}{T}}. \tag{13}$$

Both models A and B give $\frac{y_{\mathrm{Kr},2}}{y_{\mathrm{Te},3}} \gtrsim 1$ (an exception is model B at 80 d where the ratio is lower). Thus, a solar Kr/Te ratio yields a [Kr II] 1.86 μm line comparable to or stronger than [Te III] 2.20 μm, as $T \gtrsim 884$ K.

Thus, if an observed feature at 2.1 μm is assumed to be caused mainly by Te III – both models A and B, and this analysis, show that this is impossible with a solar (*r*-process component) Kr/Te ratio (at least in the ejecta component giving rise to the [Te III] 2.10 μm line); the Kr II + Kr III luminosity is always larger than that of Te III for plausible physical conditions. Krypton gives uniquely constraining information because both Kr II and Kr III have strong 2–1 lines in this spectral region. The general picture of a subsolar production of light *r*-process elements is also reinforced by the fact that quite strong predicted [Br II] 3.19 μm is not observed in AT2023vfi, with model A giving a particularly clear disagreement. A possible interpretation is that Kr and Br abundances are both significantly subsolar compared to Te.

What if Kr and Te exist in different regions, with different physical conditions? The excitation temperatures are between 6500–7700 K for these three lines. At face value, this means that also relatively small zone temperature differences could drive big differences in relative luminosities. But – if the ejecta mass is ∼0.05 $M_\odot$ and the 31–40 elements are produced in solar ratios, there must be strong Kr lines produced – as we show here equal or stronger to observed features and/or non-detections in AT2017gfo and AT2023vfi. Thus – one could boost Te by postulating that it exists in another, hotter and/or more ionized zone – but such a model would not fit the data as the Kr + Te + Se complex would be much too strong.

If subsolar production of Br and Kr is the case in the first two observed KNe, important consequences follow for the question of the origin of the light *r*-process elements. Alternative sources

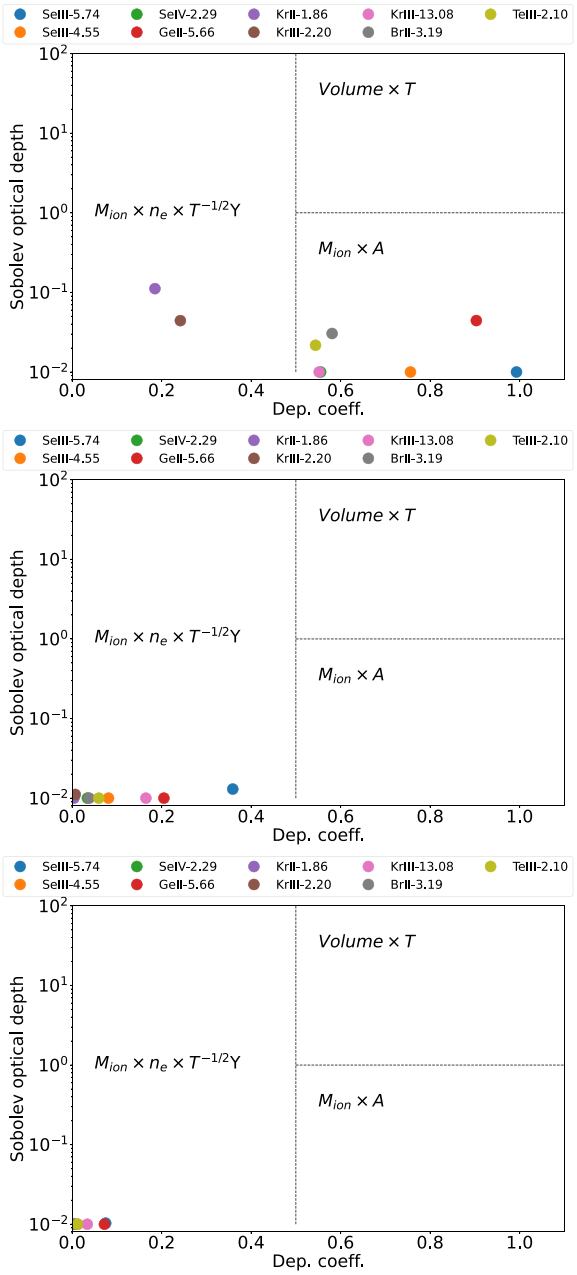

Figure 11. Formation regimes in model B at 10 d (top), 40 d (middle), and 80 d (bottom). Each point represents the zone-averaged values over the innermost eight shells. Optical depths below 10^{-2} are plotted at this floor value. The stated temperature dependencies are for the limit $T \gg T_{\rm exc}$.

for *r*-process nucleosynthesis – neutrino-driven winds in CCSNe, collapsar discs, and jets and magnetorotational SNe, in many studies appear promising for light *r*-process production (e.g. C. Travaglio et al. 2004; J. J. Cowan et al. 2021; A. Arcones & F.-K. Thielemann 2023).

At low metallicity, the weak *s*-process is not yet effective in massive stars, and therefore can their heavy element ejection be ascribed to explosive nucleosynthesis. Germanium shows no correlation with europium (Eu) in low-metallicity stars (J. J. Cowan et al. 2005), suggesting two different sources. At the same time, Ge correlates well with Fe, which suggests a coproduction. But already Se and Sr show close to solar *r*-process abundances with respect to heavier elements in several metal-poor stars (I. U. Roederer & J. E. Lawler 2012; I. U. Roederer et al. 2022). These results suggest the main *r*-process (presumably from KNe with perhaps a contribution by collapsars) is capable in making the solar *r*-process pattern from $Z = 34$.

These results appear to be in good agreement with several current KN nucleosynthesis models, which achieve patterns close to solar from $Z = 34$, but subsolar for $Z = 31 - 33$. There is however some tension with nucleosynthesis yield models for CCSNe (T. Sukhbold et al. 2016; S. Wanajo et al. 2018), which tend to give close to solar production all the way up to $Z \sim 38$ (i.e. implicating that production of these elements is small for sources producing the $Z \geq 39$ elements).

Two interesting hypothesis tests, with consideration of what the models in this paper show, now present themselves. One is that the Ge *r*-process component (estimated as 36 per cent by N. Prantzos et al. 2020) comes mainly from CCSNe. This is already a quite convincing scenario from CCSN theory, neutron-star merger theory, and low-metallicity star observations – but detections or constraining upper limits on Ge emission directly from *r*-process sources are needed to fully test this. The models here show that the hypothesis is testable with MIR observations of KNe, e.g. of the [Ge II] 5.66 μm line.

The other hypothesis is that the *r*-process components of Se, Br, and Kr (estimated at 61 per cent, 74 per cent, and 61 per cent by N. Prantzos et al. 2020) come mainly from KNe. There is tension here between CCSN theory, NSM theory, and metal-poor *r*-process enriched stars – and there is also a certain degree of tension within the KN analysis presented here. Selenium, at solar abundance, is able to roughly match the *Spitzer* photometry of AT2017gfo. On the other hand, the lack of observed Br and Kr lines suggests significantly subsolar Br and Kr production. Further *JWST* data, and yet more accurate models, hold clear promise to settle this question. There is also a close relation to the question of strontium production by KNe (D. Watson et al. 2019; N. Domoto et al. 2021; A. Perego et al. 2022; Y. Tarumi et al. 2023), as well as possible identifications of Y (A. Sneppen & D. Watson 2023) and/or Rb (Q. Pognan et al. 2023).

With the complex ejecta structures and physical formation processes, the interpretation of KN spectra is still in its infancy. Significant work has been done in the past few years to identify possible signatures, in particular in the IR where radiative transfer effects and line blending tend to be less severe. K. Hotokezaka et al. (2023) used a single-zone emissivity model where the composition is the solar one, but starting at $Z = 38$ (i.e. the abundance of Kr and other $Z < 38$ elements is zero). The physical conditions were fixed to ionization structure I − II − III − IV = 0.25, 0.4, 0.25, 0.1 for all elements, and temperature to $T = 2000$ K. The model has ejecta mass 0.05 $M_\odot$ and uniform density with $v_{\rm max} = 0.07c$ (as such the characteristic line widths are somewhere between models A and B here).

The [Te III] 2.10 μm luminosity in model A here at 10 d is significantly below the one of K. Hotokezaka et al. (2023). There are two main reasons for this. First, the Te mass fraction in the models here is 3.8 per cent (the solar value), whereas in the K. Hotokezaka et al. (2023) model it is 11 per cent; with the same total ejecta mass of 0.05 $M_\odot$ this means a factor ∼3 lower Te mass in our case. Second, our lower value for $y_{\rm Te,3}$ of ∼0.05 in model A, compared to the assumed 0.25 in K. Hotokezaka et al. (2023), combines with the 3 times lower Te mass to give a Te III mass ratio of ∼15. Both in model A here, and in the model of K. Hotokezaka

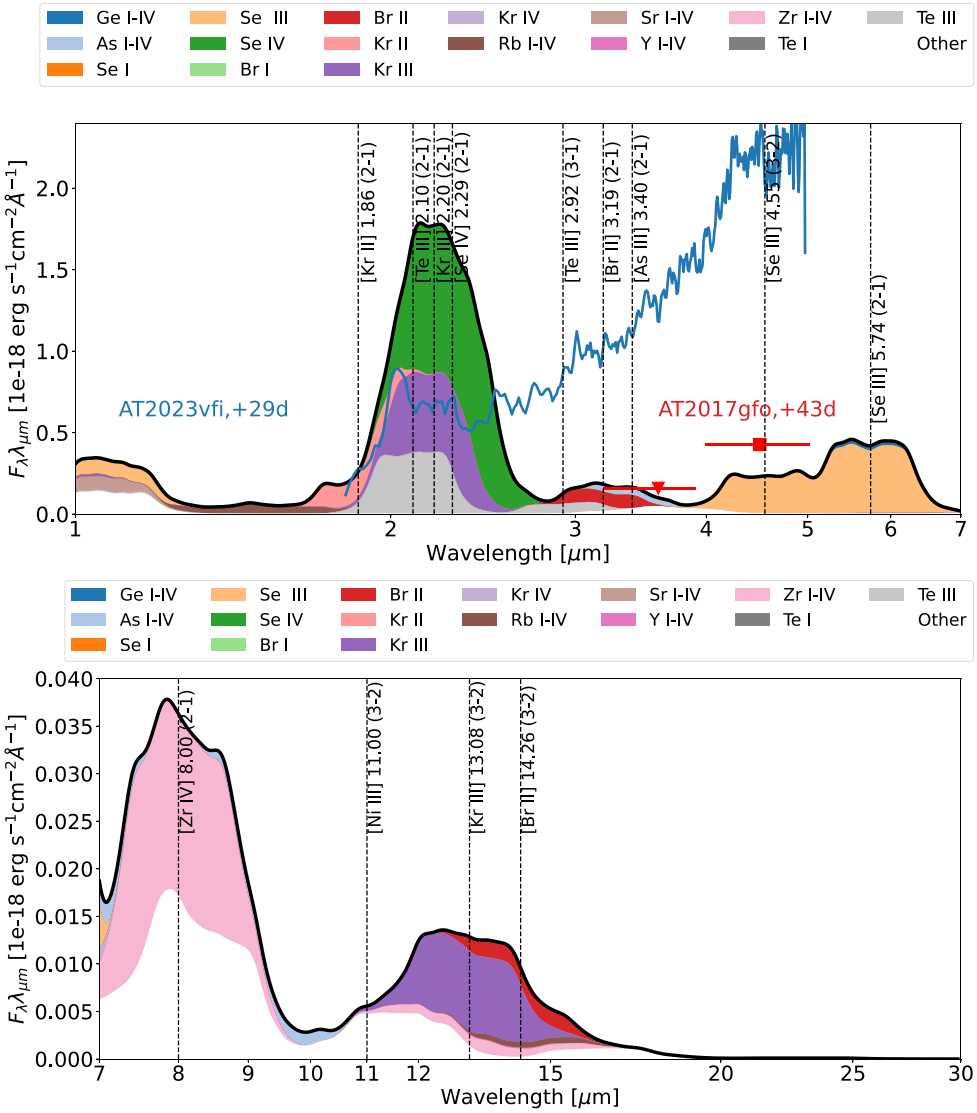

Figure 12. Spectrum of model B at 40 d, compared to the same data as in Fig. 7.

et al. (2023), electron densities are larger than $n_{e,crit}$, so the line is formed close to LTE and only ion mass and temperature affect the predicted flux. The typical temperature in model A is around 2300 K, and while this seems close to the assumed 2000 K in K. Hotokezaka et al. (2023), it leads to a factor 1.5 higher emissivity through the Boltzmann factor (entering both in LTE and NLTE limits), lowering the difference to a factor ∼10.

When the line does not form in LTE, the situation is even more complex. In model B, the much larger volume of the line-forming region leads to lower electron densities (factor ∼30), and the [Te III] 2.10 μm line forms in the transition regime between LTE and NLTE at 10 d (Fig. 11). The luminosity ratio of NLTE versus LTE emission is $L(\mathrm{NLTE})/L(\mathrm{LTE}) = n_e/n_{e,\mathrm{crit}}$, so the emission per Te III ion is lower in NLTE (as then $n_e < n_{e,\mathrm{crit}}$), all else similar. However, a higher temperature (∼4000 K) significantly brings up the Boltzmann factor (factor 3.1 from 2300 K and factor 5.1 from 2000 K), and now $y_{\mathrm{Te},3}$ has increased to $\gtrsim 0.5$, together giving a factor 35 increase for LTE emission compared to model A, and a factor 10 increase compared to K. Hotokezaka et al. (2023). But going into NLTE damps this to factors of ∼3.5 and ∼1. Finally, our lower Te mass gives a luminosity of ∼1/2 of the one of K. Hotokezaka et al. (2023).

The above analysis illustrates how the luminosity of a line can vary quite dramatically with density, composition, and energy deposition, which determine the temperature and ionization, in a model. In model A, the density to energy deposition ratio is too high to allow for sufficient Te in the doubly ionized state. In model B, it is too low, but with a lesser discrepancy.

6.1 Complementary information from Q. Pognan et al. (2026)

In Q. Pognan et al. (2026), a SUMO model grid is constructed where ejecta mass and composition (held fixed here) is varied. This grid gives complementary information about how lines can change over ejecta parameter space. One result is that for the case of no dynamic ejecta component ($f_{\mathrm{dyn}} = 0$, the composition most similar to the one used here), the spectrum is not strongly sensitive to ejecta mass, in the sense that Se I + Se III, Br I, Br II, Ni III lines are dominant for all cases at 10 d. The Ni III

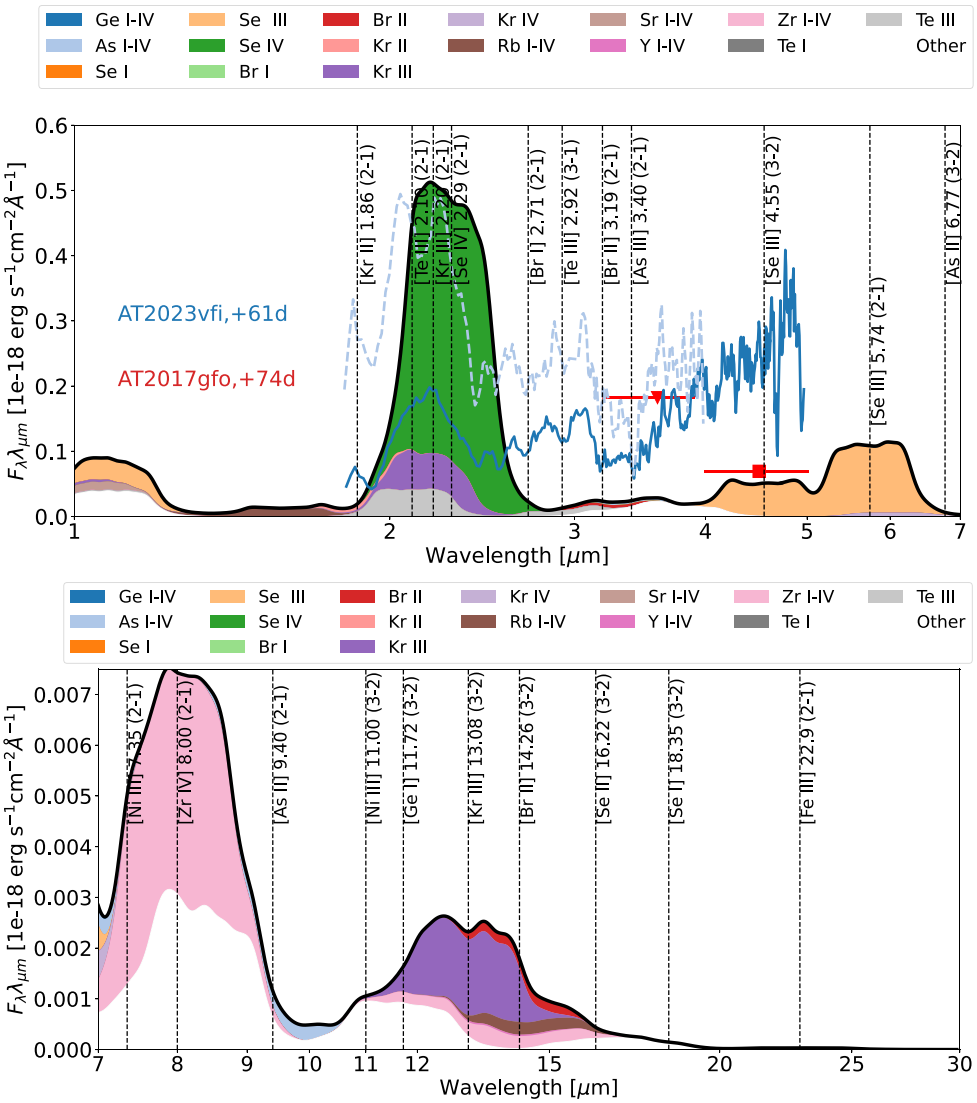

Figure 13. Spectrum of model B at 80 d, compared to the same data as in Fig. 8.

lines are stronger than here because the abundance is higher (about 7 per cent compared to 1 per cent here). The grid demonstrates that as long as mixing with heavier matter is limited (e.g. a full solar composition would have $f_{\rm dyn} \lesssim 0.1$), the light *r*-process elements still fully dominate the IR spectra – thus removing a major source of uncertainty regarding how generic results from this paper (using models with only light elements) may be taken.

Some more sensitivity is seen around the 2 μm region. The result here, that L([Kr II] 1.86 μm + [Kr III] 2.20 μm) $\gtrsim$ L([Te III] 2.10 μm) for a roughly solar Kr/Te abundances is not recovered in the Q. Pognan et al. (2026) models, despite having a ratio of ∼1.5 solar. The main reason for this is that the Q. Pognan et al. (2026) grid uses a modified Axelrod approximation for the Kr II and Kr III collision strengths; these are over a factor 10 too low compared to the calculated values used here. The line forms in NLTE in the Q. Pognan et al. (2026) models which gives direct proportionality to the collision strengths and thus a factor 10 too low Kr II and Kr III luminosities. Similarly, the [Se IV] collision strength estimate (0.16) is too low compared to the calculated 7.2 used here, leading to no or weak [Se IV] 2.29 μm line in the Q. Pognan et al. (2026) grid.

At the same time, the models here lack the $Z > 40$ elements (except Te) that also partially contribute to the 2.1 μm bump in the Q. Pognan et al. (2026) models. A full understanding of the formation of the 2.1 μm bump in AT2017gfo and AT2023vfi is clearly challenging. There are several ways such a broad bump could be generated – from a single feature dominating (for which one can directly infer the velocity of the emitting region) to blends of two or more features (where such extractions are more difficult).

7 CONCLUSIONS AND FUTURE WORK

We have studied the IR spectral signatures of light *r*-process elements ($Z \leq 40$, plus tellurium, $Z = 52$) in KNe, over the epochs 10–80 d using 1D NLTE models. We conclude the following.

(i) From the $Z = 31 - 40$ range, distinct signatures in the MIR are predicted for [Ge I] 11.72 μm, [Ge I] 17.94 μm, [Ge II] 5.66

Table 2. Summary of predicted IR lines. Models in which the line suffers significant blending are marked in parenthesis.

Ion	Line (μm)	Detectable in
Ge I	11.72	A10
	17.94	A10
Ge II	5.66	A10–80, B10
As II	6.77	A40–80
	9.40	A10–80, (B10)
As III	3.40	A40–80, (B40–B80)
Se I	5.03	A10–80
Se III	4.55	A40–80, B40–80
	5.74	(A40–80), B40–80
Se IV	2.29	(B40), B80
Br I	2.71	A10–40
Br II	3.19	A10–80, B10–40
	14.26	(A10–80), (B10–40)
Br IV	3.34	(B40–80)
	3.81	(B40–80)
Kr II	1.86	A10–80, B10–80
Kr III	2.20	(A10–80), (B10–80)
Zr I	14.91	(A40–80)
Zr II	22.28	A10
Zr III	12.42	(A10–80), (B10)
Zr IV	8.00	(B40–80)

μm, [As II] 6.77 μm, [As II] 9.40 μm, [As III] 3.40 μm, [Se I] 5.03 μm, [Se I] 18.35 μm, [Se III] 4.55 μm, [Se III] 5.74 μm, [Se IV] 2.29 μm, [Br I] 2.71 μm, [Br II] 3.19 μm, [Br II] 14.26 μm, [Kr II] 1.86 μm, [Kr III] 2.20 μm, [Kr III] 13.08 μm, and [Zr IV] 8.00 μm. In the models explored here, low-velocity ejecta (associated e.g. with a disc outflow) generate lines mainly from neutral, singly, and doubly ionized species, whereas high-velocity ejecta (associated e.g. with a hypermassive neutron star wind component) generate lines mainly from singly, doubly, and triply ionized species.

(ii) Lines evolve over time from an initially optically thick LTE regime (probing emission volume) to an optically thin NLTE regime (probing the product of ionic mass and electron density). Some lines pass through an optically thin LTE regime (directly probing ionic mass). Longer wavelength lines are less sensitive to temperature and can therefore more robustly be used to infer emission volumes and/or ionic masses.

(iii) Comparison to AT2017gfo Spitzer photometry, from $Z \leq 40$ candidates only [Se I] 5.03 μm and [Se III] 4.55 μm produce significant luminosity in the 4.5 μm band, and model predictions are in rough agreement with the observed band fluxes. Following the proposal of [Se III] 4.55 μm using models with parametrized physical conditions (K. Hotokezaka et al. 2022), these are the first self-consistent models successfully explaining this data (using a Se mass of 0.014 $M_\odot$). In the 3.6 μm band, [Br II] 3.19 μm and [As III] 3.40 μm are the dominant contributors, with fluxes at or below the upper limits.

(iv) Comparison to AT2023vfi *JWST* spectra, a light composition-only component cannot produce the smooth observed spectrum, instead giving discrete emission lines with gaps between with low flux. This may suggest that heavier elements are present that either do much of the cooling, and/or reprocess the light element emission.

(v) For a low-velocity, light-composition ejecta, [Kr II] 1.86 μm and [Kr III] 2.20 μm produce narrow, well-separated lines, inconsistent with observations of both AT2017gfo and AT2023vfi. In a higher velocity model these features partially overlap giving a bright feature centred close to 2.1 μm, as observed in both AT2017gfo and AT2023vfi. While the detailed line profile in AT2017gfo still fits better with a single line centred at 2.1 μm (with Te III 2.10 μm the leading candidate, K. Hotokezaka et al. 2023), the situation is less clear for AT2023vfi. A solar Br/Te ratio leads to predicted strong lines from [Br I] 2.71 μm and [Br II] 3.19 μm, which are not observed in AT2023vfi. The summary picture suggests that both AT2017gfo and AT2023vfi ejected significantly less light ($Z \leq 36$) *r*-process material than a solar composition. This is of interest in the context of various challenges with KNe being the main source of first *r*-process peak elements.

The results in this paper provide indications of subsolar production of light *r*-process elements in KNe. However, to more firmly establish this, progress is needed along at least three fronts.

The first is more atomic data for NLTE modelling. While the atomic data situation has significantly improved for the $Z = 31 - 40$ range in the last years (e.g. S. Banerjee et al. 2025; S. Singh et al. 2025; M. McCann et al. 2025), now enabling nebular emission modelling for both PNe and KNe with quite good accuracy, certain important data is still missing. This includes collision strengths for Ge I and II, As II and III, Se I and II, Br I, II and III, as well as recombination rates for Ge and As ions. For yet heavier elements, this kind of data are still mostly missing.

The second is improved NLTE spectral models taking into consideration deviations from spherical symmetry (being done already for the LTE phase, e.g. M. Bulla et al. 2019; C. E. Collins et al. 2023), the multicomponent nature of KNe, and doing thermalization and other microphysics to higher level of detail. While MIR lines are quite insensitive to temperature, NIR lines are more so, and there is always a direct sensitivity to ionization state. We put focus here on ratios of nearby lines of similar ions, but individual line luminosities are sensitive to physical conditions.

The third is observations of more KNe in the IR – we establish here the unique diagnostic possibilities of this range, but the data so far are very limited. Progress requires *JWST* observations with unique *r*-process signatures predicted all along the $1 - 30$ μm range.

ACKNOWLEDGEMENTS

We thank the referee for useful comments and suggestions for the manuscript. We acknowledge useful discussions with O. Just, S. Goriely, and K. Hotokezaka. We acknowledge funding from the European Research Council (ERC) under the European Union's Horizon 2020 Research and Innovation Program (ERC Starting grant 803189 – SUPERSPEC) and from the Knut and Alice Wallenberg Foundation through the "Gravity Meets Light" project. NCS acknowledges support from NSF award AST-2307116. JG thanks the Swedish Research Council for the individual starting grant with contract no. 2020-05467. The computations were enabled by resources provided by the National Academic Infrastructure for Supercomputing in Sweden (NAISS), and the Swedish National Infrastructure for Computing (SNIC), at the Parallelldatorcentrum (PDC) Center for High Performance Computing, Royal Institute of Technology (KTH), partially funded by the Swedish Research Council through grant agreements 2022-06725 and 2018-05973. We acknowledge computing funding by the Swedish Research Council (grant 2018-03799).

DATA AVAILABILITY

All computed model spectra are available upon email request to the author, and will also be made available at the Zenodo archive.

REFERENCES

Arcones A., Thielemann F.-K., 2023, A&AR, 31, 1
Axelrod T. S., 1980, PhD thesis, University of California, Santa Cruz
Badnell N. R., 1986, J. Phys. B Atom. Mol. Phys., 19, 3827
Badnell N. R., 1997, J. Phys. B Atom. Mol. Phys., 30, 1
Ballance C., 2026, Connor Ballance: Belfast atomic R-matrix codes. https://connorb.freeshell.org
Banerjee S., Jerkstrand A., Badnell N., Pognan Q., Ferguson N., Grumer J., 2025, ApJ, 992, 19
Barnes J., Zhu Y. L., Lund K. A., Sprouse T. M., Vassh N., McLaughlin G. C., Mumpower M. R., Surman R., 2021, ApJ, 918, 44
Berrington K. A., Eissner W. B., Norrington P. H., 1995, Comput. Phys. Commun., 92, 290
Biémont E., Hansen J. E., 1986a, Phys. Scr, 33, 117
Biémont E., Hansen J. E., 1986b, Phys. Scr, 34, 116
Brethauer D., Kasen D., Margutti R., Chornock R., 2026, ApJ, 996, 64
Bromley S. J., McCann M., Loch S. D., Ballance C. P., 2023, ApJS, 268, 22
Bulla M. et al., 2019, Nat. Astron., 3, 99
Collins C. E., Bauswein A., Sim S. A., Vijayan V., Martínez-Pinedo G., Just O., Shingles L. J., Kromer M., 2023, MNRAS, 521, 1858
Cowan J. J. et al., 2005, ApJ, 627, 238
Cowan J. J., Sneden C., Lawler J. E., Aprahamian A., Wiescher M., Langanke K., Martínez-Pinedo G., Thielemann F.-K., 2021, Rev. Mod. Phys., 93, 015002
Curtis S., Mösta P., Wu Z., Radice D., Roberts L., Ricigliano G., Perego A., 2023, MNRAS, 518, 5313
Dinerstein H. L., 2001, ApJ, 550, L223
Dinerstein H. L., Geballe T. R., 2001, ApJ, 562, 515
Dinerstein H. L., Lacy J. H., Sellgren K., Sterling N. C., 2006, American Astronomical Society Meeting Abstracts, p. 156.09
Dinerstein H. L., Sterling N. C., Vacca W. D., Bautista M. A., 2021, American Astronomical Society Meeting Abstracts, p. 548.13
Domoto N., Tanaka M., Wanajo S., Kawaguchi K., 2021, ApJ, 913, 26
Dougan D. J., McElroy N. E., Ballance C. P., Ramsbottom C. A., 2025, MNRAS, 541, 367
Eriksson K. B. S., 1974, J. Opt. Soc. Am., 64, 1272
Ferland G. J., 2003, ARA&A, 41, 517
Fernández R., Metzger B. D., 2013, MNRAS, 435, 502
Fernández R., Just O., Xiong Z., Martínez-Pinedo G., 2024, Phys. Rev. D, 110, 023001
Fujibayashi S., Shibata M., Wanajo S., Kiuchi K., Kyutoku K., Sekiguchi Y., 2020a, Phys. Rev. D, 101, 083029
Fujibayashi S., Wanajo S., Kiuchi K., Kyutoku K., Sekiguchi Y., Shibata M., 2020b, ApJ, 901, 122
Fujibayashi S., Kiuchi K., Wanajo S., Kyutoku K., Sekiguchi Y., Shibata M., 2023, ApJ, 942, 39
Gillanders J. H., Smartt S. J., 2025, MNRAS, 538, 1663
Gillanders J. H. et al., 2023, preprint (arXiv:2308.00633)
Gillanders J. H., Sim S. A., Smartt S. J., Goriely S., Bauswein A., 2024, MNRAS, 529, 2918
Goriely S., 1999, A&A, 342, 881
Goriely S., Bauswein A., Just O., Pllumbi E., Janka H. T., 2015, MNRAS, 452, 3894
Haas M. R., Colgan S. W. J., Erickson E. F., Lord S. D., Burton M. G., Hollenbach D. J., 1990, ApJ, 360, 257
Hjorth J. et al., 2017, ApJ, 848, L31
Hotokezaka K., Tanaka M., Kato D., Gaigalas G., 2021, MNRAS, 506, 55863
Hotokezaka K., Tanaka M., Kato D., Gaigalas G., 2022, MNRAS, 515, L89
Hotokezaka K., Tanaka M., Kato D., Gaigalas G., 2023, MNRAS, 526, L155
Jerkstrand A., 2017, in Alsabti A. W., Murdin P., eds, Handbook of Supernovae. Springer International Publishing AG, 795
Jerkstrand A., 2025, Living Rev. Comput. Astrophys., 11, 1
Jerkstrand A., Fransson C., Kozma C., 2011, A&A, 530, A45
Jerkstrand A., Fransson C., Maguire K., Smartt S., Ergon M., Spyromilio J., 2012, A&A, 546, A28
Jerkstrand A., Ergon M., Smartt S. J., Fransson C., Sollerman J., Taubenberger S., Bersten M., Spyromilio J., 2015, A&A, 573, A12
Joshi Y. N., Budhiraja C. J., 1971, Can. J. Phys., 49, 670
Just O., Bauswein A., Ardevol Pulpillo R., Goriely S., Janka H.-T., 2015, MNRAS, 448, 541
Just O., Goriely S., Janka H. T., Nagataki S., Bauswein A., 2022, MNRAS, 509, 1377
Just O. et al., 2023, ApJ, 951, L12
Kasen D., Barnes J., 2019, ApJ, 876, 128
Kasliwal M. M. et al., 2022, MNRAS, 510, L7
Kawaguchi K., Fujibayashi S., Shibata M., Tanaka M., Wanajo S., 2021, ApJ, 913, 100
Kiuchi K., Fujibayashi S., Hayashi K., Kyutoku K., Sekiguchi Y., Shibata M., 2023, Phys. Rev. Lett., 131, 011401
Kotak R. et al., 2006, ApJ, 651, L117
Kotak R. et al., 2009, ApJ, 704, 306
Levan A. J. et al., 2024, Nature, 626, 737
Macaluso D. A. et al., 2019, J. Phys. B Atom. Mol. Phys., 52, 145002
Madonna S. et al., 2018, ApJ, 861, L8
McCann M., Ballance C. P., McNeill F., Sim S. A., Ramsbottom C. A., 2025, MNRAS, 540, 2923
McLaughlin B. M., Babb J. F., 2019, J. Phys. B Atom. Mol. Phys., 52, 125201
Metzger B. D., Fernández R., 2014, MNRAS, 441, 3444
Moore C. E., 1971, Nat. Stand. Ref. Data Ser., NSRDS-NBS 35, Vol. II (Reprint of NBS Circ. 467, Vol. II, 1952). Nat. Bur. Stand., Gaithersburg, MD
Morillon C., Vergès J., 1975, Phys. Scr., 12, 145
Moseley S. H., Dwek E., Glaccum W., Graham J. R., Loewenstein R. F., Silverberg R. F., 1989, ApJ, 347, 1119
Mulholland L. P., McElroy N. E., McNeill F. L., Sim S. A., Ballance C. P., Ramsbottom C. A., 2024a, MNRAS, 532, 2289
Mulholland L. P., McNeill F., Sim S. A., Ballance C. P., Ramsbottom C. A., 2024b, MNRAS, 534, 3423
Mulholland L. P., Bromley S. J., Ballance C. P., Sim S. A., Ramsbottom C. A., 2025, J. Quant. Spec. Radiat. Transf., 345, 109545
Nilsson A. E., Johansson S., Kurucz R. L., 1991, Phys. Scr, 44, 226
Palmer B. A., 1977 Ph.D. Thesis, Purdue Univ., Purdue
Pequignot D., Baluteau J. P., 1994, A&A, 283, 593
Perego A. et al., 2022, ApJ, 925, 22
Persson W., 1978, Phys. Scr, 17, 387
Pian E. et al., 2017, Nature, 551, 67
Pognan Q., Jerkstrand A., Grumer J., 2022a, MNRAS, 510, 3806
Pognan Q., Jerkstrand A., Grumer J., 2022b, MNRAS, 513, 5174
Pognan Q., Grumer J., Jerkstrand A., Wanajo S., 2023, MNRAS, 526, 5220
Pognan Q., Wu M.-R., Martínez-Pinedo G., da Silva R. F., Jerkstrand A., Grumer J., Flörs A., 2025, MNRAS, 536, 2973
Pognan Q., Kawaguchi K., Wanajo S., Fujibayashi S., Jerkstrand A., Grumer J., 2026, MNRAS, 457, 3,
Prantzos N., Abia C., Cristallo S., Limongi M., Chieffi A., 2020, MNRAS, 491, 1832
Rastinejad J. C., Fong W., Kilpatrick C. D., Nicholl M., Metzger B. D., 2025, ApJ, 979, 190
Reader J., Acquista N., 1997, Phys. Scr., 55, 310
Ricigliano G., Hotokezaka K., Arcones A., 2025, MNRAS, 543, 2534
Roederer I. U., Lawler J. E., 2012, ApJ, 750, 76
Roederer I. U. et al., 2022, ApJS, 260, 27
Rynkun P., Gaigalas G., Jönsson P., 2020, A&A, 637, A10
Sahoo B. K., Nataraj H. S., Das B. P., Chaudhuri R. K., Mukherjee D., 2008, J. Phys. B Atom. Mol. Phys., 41, 055702
Saloman E. B., 2007, J. Phys. Chem. Ref. Data, 36, 215
Sansonetti J. E., 2006, J. Phys. Chem. Ref. Data, 35, 301
Sansonetti J. E., Nave G., 2010, J. Phys. Chem. Ref. Data, 39, 033103
Schöning T., 1997, A&AS, 122, 277

Shirai T., Reader J., Kramida A. E., Sugar J., 2007, J. Phys. Chem. Ref. Data, 36, 509
Singh S., Harman Z., Keitel C. H., 2025, A&A, 700, A110
Smartt S. J. et al., 2017, Nature, 551, 75
Sneppen A., Watson D., 2023, A&A, 675, A194
Sneppen A., Damgaard R., Watson D., Collins C. E., Shingles L., Sim S. A., 2024, A&A, 692, A134
Sterling N. C., 2011, A&A, 533, A62
Sterling N. C., Witthoeft M. C., 2011, A&A, 529, A147
Sterling N. C., Dinerstein H. L., Kallman T. R., 2007, ApJS, 169, 37
Sterling N. C., Porter R. L., Dinerstein H. L., 2015, ApJS, 218, 25
Sterling N. C., Dinerstein H. L., Kaplan K. F., Bautista M. A., 2016, ApJ, 819, L9
Sterling N. C., Madonna S., Butler K., García-Rojas J., Mashburn A. L., Morisset C., Luridiana V., Roederer I. U., 2017, ApJ, 840, 80
Sugar J., Corliss C., 1985, Atomic Energy Levels of the Iron-period Elements: Potassium Through Nicke. American Chemical Society, Washington
Sugar J., Musgrove A., 1993, J. Phys. Chem. Ref. Data, 22, 1213
Sugar J., Musgrove A., 1995, J. Phys. Chem. Ref. Data, 24, 1803
Sukhbold T., Ertl T., Woosley S. E., Brown J. M., Janka H. T., 2016, ApJ, 821, 38
Tanaka M. et al., 2017, PASJ, 69, 102
Tarumi Y., Hotokezaka K., Domoto N., Tanaka M., 2023, preprint (arXiv:2302.13061)
Tech J. L., 1963, J. Res. Natl. Bur. Stand. (U.S.), Sect. A, 67, 505
Travaglio C., Gallino R., Arnone E., Cowan J., Jordan F., Sneden C., 2004, ApJ, 601, 864
Vieira N., Ruan J. J., Haggard D., Drout M. R., Fernández R., 2026, ApJ, 997, 92
Villar V. A. et al., 2017, ApJ, 851, L21
Villar V. A. et al., 2018, ApJ, 862, L11
Wanajo S., Sekiguchi Y., Nishimura N. Kiuchi K., Kyutoku K., Shibata M., 2014, ApJ, 789, L39
Wanajo S., Müller B., Janka H.-T., Heger A., 2018, ApJ, 852, 40
Watson D. et al., 2019, Nature, 574, 497
Waxman E., Ofek E. O., Kushnir D., 2019, ApJ, 878, 93
Wollaeger R. T. et al., 2018, MNRAS, 478, 3298
Wooden D. H., Rank D. M., Bregman J. D., Witteborn F. C., Tielens A. G. G. M., Cohen M., Pinto P. A., Axelrod T. S., 1993, ApJS, 88, 477
Yang Y.-H. et al., 2024, Nature, 626, 742

APPENDIX A: ATOMIC DATA UPDATES

The dielectronic recombination rates calculated for Se, Rb, Sr, Y, and Zr by S. Banerjee et al. (2025) and Kr (N. C. Sterling 2011) were used. The dielectronic and radiative recombination rates for Br and the radiative recombination rates for Rb, from Kerlin et al. (in preparation), were also incorporated.

As outlined in more detail below, some energy levels in our FAC base-set (Q. Pognan et al. 2023) were corrected to experimental values or, lacking that, to more accurate theoretical ones. In such calibrations, lines connecting to the level had A-values rescaled by a factor $(\lambda_{\rm old}/\lambda_{\rm new})^3$ (K. Hotokezaka et al. 2021). The numbering of levels in the descriptions below refer to the energy-ordering in the FAC model atoms [using a spectroscopic configuration-interaction (SCI) method, Q. Pognan et al. 2023].

A1 Ga I

The energy of level 2 ($^2P^o_{3/2}$) was corrected to values from the National Institute of Standards and Technology NIST (T. Shirai et al. 2007). The Ga I isoelectronic sequence (Ga I, Ge II, As III, Se IV, etc.) has a single p-shell valence electron, giving a doublet ground term ^{2}P with $J = 3/2$ or $J = 1/2$ depending on the spin of the electron. A potential IR line is therefore $^2P^o_{3/2}$–$^2P^o_{1/2}$ (2–1, 12.10 μm, $A = 4.6 \times 10^{-3}$ s^{-1}).

A2 Ga II

The first excited state in Ga II lies high at 47 367 cm^{-1}, no calibrations were made. The Ga II isoelectronic sequence (Zn I, Ga II, Ge III, As IV, etc.) has a 4s^2 ground configuration with no fine structure splitting.

A3 Ga III

The first excited state in Ga III lies high at at 65 169 cm^{-1}, no calibrations were made. The Ga III isoelectronic sequence (Cu I, Zn II, Ga III, Ge IV, etc.) has a single-electron (4s) ground configuration.

A4 Ga IV

The first excited state in Ga IV lies high at 149 512 cm^{-1}, no calibrations were made. The Ga IV isoelectronic sequence (Cu II, Zn III, Ga IV, etc.[4]) has a 3d^{10}(^{1}S) ground configuration with no splitting.

A5 Ge I

The energies for levels 2–5 ($^3P_1$, $^3P_2$, $^1D_2$, $^1S_0$) were corrected to NIST values (J. Sugar & A. Musgrove 1993). Theoretical A-values for transitions between these first five levels are provided by E. Biémont & J. E. Hansen (1986a, Hartree-plus-statistical-exchange and Hartree–Fock with relativistic corrections). The Ge I isoelectronic sequence (Ge I, As II, Se III, Br IV, etc.) has two p-shell electrons. In the ground term the spins are aligned (so $2S + 1 = 3$); and splitting occurs by three allowed values for the orbital magnetic number giving $J = 2, 1, 0$. Transitions with $\Delta J = 1$ have significantly higher A-values than $\Delta J = 2$, giving two main lines from the ground term. Potential IR lines are $^3P_1$–$^3P_0$ (2–1, 17.94 μm, $A = 3.3 \times 10^{-3}$ s^{-1}), $^3P_2$–$^3P_1$ (3–2, 11.72 μm, $A = 8.0 \times 10^{-3}$ s^{-1}), and (trans-term) $^1D_2$–$^3P_0$ (4–3, 1.75 μm, $A = 0.098$ s^{-1}).

A6 Ge II

The energy of level 2 ($^2P^o_{3/2}$) was corrected to NIST (J. Sugar & A. Musgrove 1993). A potential IR line is $^2P^o_{3/2}$–$^2P^o_{1/2}$ (2–1, 5.66 μm, $A = 0.050$ s^{-1}).

A7 Ge III

The first excited state in Ge III lies high at 61 733 cm^{-1}, no calibrations were made.

A8 Ge IV

The first excited state in Ge IV lies high at 81 311 cm^{-1}, no calibrations were made.

[4]Ni I breaks pattern with a different ground term, 3d^8(^{3}F)4s^2.

A9 As I

The energies of levels 2–5 ($^2D^o_{3/2}$, $^2D^o_{5/2}$, $^2P^o_{1/2}$, $^2P^o_{3/2}$) were corrected to NIST values (C. E. Moore 1971). Theoretical A-values for transitions between the first five levels are provided by E. Biémont & J. E. Hansen (1986a, their table 6). The As I isoelectronic sequence (As I, Se II, Br III, Kr IV, etc.) has a $4p^3(^4S)$ ground configuration with no splitting. IR lines can only be generated from the second term, $4p^3(^2D^o)$. For As I the $^2D^o_{5/2}$–$^2D^o_{3/2}$ transition is however beyond *JWST* range at 31 μm, and with a low A-value.

A10 As II

The energies of levels 2–5 ($^3P_1$, $^3P_2$, $^1D_2$, $^1S_0$) were corrected to NIST values (C. E. Moore 1971). Theoretical A-values for transitions between the first five levels are provided by E. Biémont & J. E. Hansen (1986a). Potential IR lines include $^3P_1$–$^3P_0$ (2–1, 9.40 μm, $A = 0.022\ s^{-1}$) and $^3P_2$–$^3P_1$ (3–2, 6.77 μm, $A = 0.043\ s^{-1}$).

A11 As III

The energy of level 2 ($^2P^o_{3/2}$) was corrected to the NIST value (C. E. Moore 1971). A potential IR line is $^2P^o_{3/2}$–$^2P^o_{1/2}$ (2–1, 3.40 μm, $A = 0.23\ s^{-1}$.)

A12 As IV

The first excited state in As IV lies high at 75 812 cm^{-1}, no calibrations were made.

A13 Se I

The energies of levels 2–5 ($^3P_1$, $^3P_0$, $^1D_2$, $^1S_0$) were corrected to NIST values (C. E. Moore 1971). Theoretical A-values for transitions between the first five levels are provided by E. Biémont & J. E. Hansen (1986b, Hartree–Fock with relativistic corrections, their table 8). The Se I isoelectronic sequence (Se I, Br II, Kr III, Rb IV, etc.) has a $4p^4(^3P)$ ground term with $J = 2, 1, 0$ splitting. Potential IR lines include $^3P_1$–$^3P_2$ (2–1, 5.03 μm, $A = 0.17\ s^{-1}$), $^3P_0$–$^3P_1$ (3–2, 18.35 μm, $A = 0.010\ s^{-1}$), and (trans-term) $^1D_2$–$^3P_2$ (4–1, 1.04 μm, $A = 0.63\ s^{-1}$).

A14 Se II

The energies of levels 2–5 ($^2D^o_{3/2}$, $^2D^o_{5/2}$, $^2P^o_{1/2}$, $^2P^o_{3/2}$) were corrected to NIST values (C. E. Moore 1971). Theoretical A-values for transitions between the first five levels are provided by E. Biémont & J. E. Hansen (1986a, their table 6). The $^2D^o_{5/2}$–$^2D^o_{3/2}$ transition (within the second term) is at 16.22 μm, with $A = 2.9 \times 10^{-3}\ s^{-1}$.

A15 Se III

The energies of levels 2–5 ($^3P_1$, $^3P_2$, $^1D_2$, $^1S_0$) were corrected to NIST values (C. E. Moore 1971). Theoretical A-values for transitions between the first five levels are provided by E. Biémont & J. E. Hansen (1986a) and N. C. Sterling et al. (2017), we use the latter source as it also reports R-matrix calculations of collision strengths for these transitions, which we use. Potentially important IR lines include $^3P_2$-$^3P_1$ (3–2, 4.55 μm, $A = 0.16\ s^{-1}$), and $^3P_1$-$^3P_0$ (2–1, 5.74 μm, $A = 0.082\ s^{-1}$).

A16 Se IV

Level 2 ($^2P^o_{3/2}$) was corrected to the NIST value (C. E. Moore 1971). Collision strengths for this transition were implemented (N. C. Sterling, H. L. Dinerstein & T. R. Kallman 2007, K. Butler, private communication). A potential IR line is $^2P^o_{3/2}$–$^2P^o_{1/2}$ (2–1, 2.29 μm, $A = 0.75\ s^{-1}$).

A17 Br I

Level 2 ($^2P_{1/2}$) was corrected to the NIST value (J. L. Tech 1963). The Br I isoelectronic sequence (Br I, Kr II, Rb III, Sr IV, etc.) has a $4p^5(^2P)$ ground term with $J = 3/2, 1/2$ splitting. A potential IR line is $^2P_{1/2}$ –^{2} $P_{3/2}$ (2–1, 2.71 μm, $A = 0.90\ s^{-1}$).

A18 Br II

The energies of levels 2–5 ($^3P_1$, $^3P_0$, $^1D_2$, $^1S_0$) were corrected to NIST values (C. E. Moore 1971). Theoretical A-values for transitions between the first five levels are provided by E. Biémont & J. E. Hansen (1986b, their table 8). Potential IR lines include $^3P_1$–$^3P_0$ (2–1, 3.19 μm, $A = 0.67\ s^{-1}$) and $^3P_0$–$^3P_1$ (3–2, 14.26 μm, $A = 0.022\ s^{-1}$).

A19 Br III

The energies of levels 2–5 ($^2D^o_{3/2}$, $^2D^o_{5/2}$, $^2P^o_{1/2}$, $^2P^o_{3/2}$) were corrected to NIST values (C. E. Moore 1971). A potential IR line is (second-term) $^2D^o_{5/2}$–$^2D^o_{3/2}$ (3–2, 7.94 μm, $A = 2.0 \times 10^{-2}\ s^{-1}$).

A20 Br IV

The energies of levels 2–4 ($^3P_1$, $^3P_2$, $^1D_2$) were corrected to NIST values (Y. N. Joshi & C. J. Budhiraja 1971). Theoretical A-values for transitions between the first five levels are provided by E. Biémont & J. E. Hansen (1986a). Potential IR lines include $^3P_1$–$^3P_0$ (2–1, 3.81 μm, $A = 0.32\ s^{-1}$) and $^3P_2$–$^3P_1$ (3–2, 3.34 μm, $A = 0.33\ s^{-1}$).

A21 Kr I

The first excited state of Kr I lies high at 79 971 cm^{-1}, no calibrations were made. The Kr I isoelectronic sequence (Kr I, Rb II, Sr III, Y IV, etc.) has a $4p^6(^1S)$ ground term with no splitting.

A22 Kr II

The energy of level 2 ($^2P_{1/2}$) was corrected to the NIST value (E. B. Saloman 2007). The third state lies high at 109 000 cm^{-1}. A potential IR line is $^2P_{1/2}$–$^2P_{3/2}$ (2–1, 1.86 μm, $A = 2.78\ s^{-1}$).

Collision strengths were computed for the 2–1 transition, using a 70 state Breit–Pauli R-Matrix (BPRM) calculation. This is similar to the calculations by L. P. Mulholland et al. (2024a) for Sr II and Y II and we refer the interested reader to that paper for further details of and references to the methods. The Kr II target wavefunctions were computed using AUTOSTRUCTURE (N. R. Badnell 1997, 1986) with seven configurations ($4s^24p^5$, $4s4p^6$, $4s^24p^44d$, $4s^24p^44f$, $4s^24p^45s$, $4s^24p^45p$, $4s^24p^45d$) being included in the configuration expansion. The radial wavefunctions were optimized by minimizing the sum of the energies of the lowest 30 LS-coupling terms which gave the following values

for the parameters of the Thomas–Fermi–Dirac–Amaldi potential: $\lambda_{1s} = 1.4240$, $\lambda_{2s} = 1.1393$, $\lambda_{2p} = 1.0856$ $\lambda_{3s} = 1.0385$, $\lambda_{3p} = 1.0207$, $\lambda_{3d} = 1.0005$ $\lambda_{4s} = 0.9913$, $\lambda_{4p} = 1.0039$, $\lambda_{4d} = 1.0424$ $\lambda_{4f} = 1.0483$, $\lambda_{5s} = 1.0015$, and $\lambda_{5p} = 0.9934$ $\lambda_{5d} = 1.0062$. The BPRM calculation itself was performed using the BELFAST codes (K. A. Berrington, W. B. Eissner & P. H. Norrington 1995) in versions maintained by Dr. Connor Ballance which are to be found at C. Ballance (2026). J values up to 37 were included explicitly, while larger values were estimated via a 'top-up' procedure. The energy grid included of order 15 000 points up to the highest threshold (approximately 1.554 Ryd) with a further 860 points to extend the grid up to roughly 10 Ryd. This was augmented with the infinity energy point provided by AUTOSTRUCTURE. The resulting cross-sections were convolved with a Maxwellian distribution and are available in adf04 format.

A23 Kr III

The energies of levels 2–5 ($^3P_1$, $^3P_0$, $^1D_2$, $^1S_0$) were corrected to the NIST values (E. B. Saloman 2007). Theoretical A-values for transitions between the first five levels are provided by E. Biémont & J. E. Hansen (1986b, their table 8). T. Schöning (1997) provide R-matrix calculations of collision strengths. Potential IR lines include $^3P_1$–$^3P_2$ (2–1, 2.20 μm, $A = 2.0$ s^{-1}) and $^3P_0$–$^3P_1$ (3–2, 13.08 μm, $A = 0.029$ s^{-1}).

A24 Kr IV

The energies of levels 2–5 ($^2D^o_{3/2}$, $^2D^o_{5/2}$, $^2P^o_{1/2}$, $^2P^o_{3/2}$) were corrected to NIST values (E. B. Saloman 2007). T. Schöning (1997) provide R-matrix calculations of collision strengths. A potential IR line is (second-term) $^2D^o_{5/2}$–$^2D^o_{3/2}$ (3–2, 6.01 μm, $A = 0.046$ s^{-1}).

A25 Rb I

The energies of levels 2–6 ($^2P^o_{1/2}$, $^2P^o_{3/2}$, $^2D_{5/2}$, $^2D_{3/2}$, $^2S_{1/2}$) were corrected to NIST values (J. E. Sansonetti 2006), which included a reordering of levels 4-6. Rb I has no expected strong IR lines. Rb I has a single-electron 5s(^{2}S) ground state.

A26 Rb II

The first excited state of Rb II lies high at 133 341 cm^{-1}, no calibrations were made.

A27 Rb III

The energy of level 2 ($^2P_{1/2}$) was corrected to the NIST value (J. E. Sansonetti 2006). The third level lies high at 130 032 cm $^{-1}$. A potential IR line is $^2P_{1/2}$–$^2P_{3/2}$ (2–1, 1.36 μm, $A = 7.21$ s^{-1}).

A28 Rb IV

The energies of levels 2–5 ($^3P_1$, $^3P_0$, $^1D_2$, $^1S_0$) were corrected to NIST values (J. E. Sansonetti 2006). Theoretical A-values for transitions between the first five levels are provided by E. Biémont & J. E. Hansen (1986b, their table 8). We use collision strengths for the first five levels from N. C. Sterling et al. (2016).[5] Potential IR lines include $^3P_1$–$^3P_2$ (2–1, 1.60 μm, $A = 4.65$ s^{-1}) and $^3P_0$–$^3P_1$ (3–2, 14.54 μm, $A = 2.3 \times 10^{-2}$ s^{-1}).

A29 Sr I

The energies of levels 2–9 ($^3P^o_{0,1,2}$, $^3D_{1,2,3}$, $^1D_2$, $^1P^o_1$) were corrected to NIST values (J. E. Sansonetti & G. Nave 2010), which involved some reorderings. Sr I has a 5s^2(^{1}S) ground term with no splitting.

A30 Sr II

The energies of levels 2–17 ($^2D_{5/2,3/2}$, $^2P^o_{1/2,3/2}$, $^2S_{1/2}$, 5d($^2D_{5/2,3/2}$), 6p($^2P^o_{1/2,3/2}$), $^2F^o_{7/2,5/2}$, 7s($^2S_{1/2}$), 6d($^2D_{3/2,5/2}$), 7p($^2P^o_{1/2,3/2}$)) were corrected to NIST values (C. E. Moore 1971). Collision strengths from L. P. Mulholland et al. (2024a) were used.

A31 Sr III

The first excited state of Sr III lies high at 176 434 cm^{-1}, no calibrations were made.

A32 Sr IV

The energy of level 2 ($^2P_{1/2}$) was corrected to the NIST value (W. Persson 1978). A potential IR line is $^2P_{1/2}$–$^2P_{3/2}$ (2–1, 1.028 μm, $A = 15.8$ s^{-1}).

A33 Y I

The energies of levels 2–8 (a^{2}D$_{5/2}$, z^{2}P$^o_{1/2,3/2}$, a^{4}F$_{3/2,5/2,7/2,9/2}$) were corrected to NIST values (B. A. Palmer 1977), which involved some reorderings. Because the FAC energy structure is significantly different to the NIST one for higher levels, the model atom was limited to these eight states. Y I has a 4d5s^2(^{2}D) ground configuration with splitting into $J = 3/2, 5/2$ (Zr II, Nb III, etc. have other ground configurations so the isoelectronic sequencing here breaks down). A potential IR line is $^2D_{5/2}$–$^2D_{3/2}$ (2–1, 18.85 μm, $A = 5.5 \times 10^{-4}$ s^{-1}).

A34 Y II

The energies of levels 2–12 (a^{3}D$_{1,2,3}$, a^{1}D$_2$, a^{3}F$_{2,3,4}$, a^{3}P$_{0,1,2}$, b^{1}D$_2$) were corrected to NIST values (A. E. Nilsson, S. Johansson & R. L. Kurucz 1991). We implemented collision strengths for transitions between the first 12 levels from L. P. Mulholland et al. (2024a). Y II has a 5s^2(^{1}S) ground term with no splitting. However, it has a rich level structure of quite low-energy metastable states, difficult to assess beforehand if IR lines from these may become strong.

A35 Y III

The energies of levels 2–17 were in Q. Pognan et al. (2023) calibrated to NIST values. Here, we also add A-values for transitions between the first three states from B. K. Sahoo et al. (2008). Y III has a 4p^6(^{2}D) ground term with $J = 3/2, 5/2$ splitting. Potential IR lines include $^2D_{5/2}$–$^2D_{3/2}$ (2–1, 13.81 μm, $A = 4.1 \times 10^{-3}$ s^{-1}), 5s^2S–4d^2D$_{3/2}$ (3–1, 1.34 μm, $A = 9.4 \times 10^{-2}$ s^{-1}), and 5s^2S–4d^2D$_{5/2}$ (3–2, 1.48 μm, $A = 4.5 \times 10^{-2}$ s^{-1}).

[5] N. C. Sterling et al. (2016) also compute A-values, but list zero for several transitions that have non-zero entries in E. Biémont & J. E. Hansen (1986b). In their discussion they also use the E. Biémont & J. E. Hansen (1986b) values as benchmark.

A36 Y IV

The first excited state in Y IV lies high at 209 651 cm^{-1}, no calibrations were made.

A37 Zr I

The energies of levels 2–12 ($a^3F_{3,4}$, $a^3P_{2,0,1}$, $a^5F_{1,2,3,4,5}$, a^1D_2, a^1G_4) were corrected to NIST values (C. E. Moore 1971). Potential IR lines include $^3F_3-^3F_2$ (2–1, 17.53 μm, $A = 3.2 \times 10^{-3}$ s^{-1}), $^3F_4-^3F_3$ (3–2, 14.91 μm, $A = 4.7 \times 10^{-3}$ s^{-1}), and a blend of lines between 2 − 2.5 μm.

A38 Zr II

The energies of levels 2–4 ($a^4F_{5/2,7/2,9/2}$) were corrected to NIST values (C. E. Moore 1971). Potential MIR lines include $^4F_{9/2}-^4F_{7/2}$ (4–3, 17.87 μm, $A = 2.7 \times 10^{-3}$ s^{-1}) and $^4F_{7/2}-^4F_{5/2}$ (3–2, 22.28 μm, $A = 2.1 \times 10^{-3}$ s^{-1}).

A39 Zr III

The energies of levels 2–13 ($^3F_{3,4}$, $^1D_2$, $^3P_{0,1,2}$, $^1G_4$, $^3D_{1,2,3}$, $^1S_0$, $^1D_2$) were corrected to NIST values (J. Reader & N. Acquista 1997). We also replaced the FAC A-values for transitions between these states with those of P. Rynkun, G. Gaigalas & P. Jönsson (2020, multi-configuration Dirac–Hartree–Fock and relativistic configuration interaction calculations using GRASP2018). Potential IR lines include $^3F_3-^3F_2$ (2–1, 14.67 μm, $A = 7.5 \times 10^{-3}$ s^{-1}) and $^3F_4-^3F_3$ (3–2, 12.42 μm, $A = 1.0 \times 10^{-2}$ s^{-1}).

A40 Zr IV

The energies of levels 2–5 ($^2D_{5/2}$, $^2S_{1/2}$, $^2P^o_{1/2,3/2}$) were corrected to NIST values (J. Reader & N. Acquista 1997). Level 6 lies high at 137 413 cm^{-1}. Collision strengths for transitions between these first five levels were implemented (H. L. Dinerstein et al. 2006, K. Butler, private communication). A potential IR line is $^2D_{5/2}-^2D_{3/2}$ (2–1, 8.00 μm, $A = 0.012$ s^{-1}).

A41 Te I

The energies of levels 2–10 ($^3P_{0,1}$, $^1D_2$, $^1S_0$, $^5S^o_2$, $^3S^o_1$, $^5P_{1,2,3}$) were calibrated to NIST values (C. Morillon & J. Vergès 1975). Because higher levels showed discrepancy between the FAC model and NIST, the model atom was capped at 10 levels – the 11th level lies quite high at 54 683 cm^{-1}. We use collision strengths from L. P. Mulholland et al. (2024b). A potential IR line is $^3P_1-^3P_2$ (3–1, 2.10 μm, $A = 2.27$ s^{-1}).

A42 Te II

The energies of levels 2–8 ($^2D^o_{3/2,5/2}$, $^2P^o_{1/2,3/2}$, $^4P_{5/2,3/2,1/2}$) were calibrated to NIST values (K. B. S. Eriksson 1974). Because higher levels showed discrepancy between the FAC model and NIST, the model atom was capped at eight levels – the ninth level lies high at 78 448 cm^{-1}. A potential IR line is $^2D^o_6-^2D^o_4$ (3–2, 4.55 μm, $A = 0.098$ s^{-1}).

A43 Te III

The energies of levels 2–4 ($^3P_{1,2}$, $^1D_2$) were calibrated to NIST values (C. E. Moore 1971). Because higher levels showed discrepancy between the FAC model and NIST, the model atom was capped at four levels – the fifth level lies high at 82 885 cm^{-1}. A-values and collision strengths from S. Madonna et al. (2018) were used. Potential IR lines include $^3P_1-^3P_0$ (2–1, 2.10 μm, $A = 1.19$ s^{-1}) and $^3P_2-^3P_1$ (3–2, 2.92 μm, $A = 0.52$ s^{-1}).

A44 Te IV

The energy of level 2 ($^2P^o_{3/2}$) was calibrated to NIST values (C. E. Moore 1971). Because higher levels showed discrepancy between the FAC model and NIST, the model atom was capped at two levels – the third level lies high at 92 772 cm^{-1}. A potential IR line is $^2P^o_{3/2}-^2P^o_{1/2}$ (2–1, 1.084 μm, $A = 7.1$ s^{-1}).

A45 Fe, Ni, and Zn

For Fe I–III and Ni I–Ni III, we used the standard atomic data set in SUMO. For this study, we added also a two-level atom for Fe IV and a seven-level model atom for Ni IV (J. Sugar & C. Corliss 1985). For Zn I–IV, we use the FAC model set, with energy calibrations done for the first few levels of each ion (J. Sugar & A. Musgrove 1995). The only significant IR line candidate from zinc is from [Zn IV] 3.62 μm.

APPENDIX B: SENSITIVITY TO DEPOSITION POWER

In Fig. B1, we compare the model spectra when power levels change. In the top panel, f changes from 1 to 6 in model A at 10 d. The general temperature rise causes an increase in flux below ~ 4 μm. The changes after that are driven solely by ionization changes, as the lines become temperature-insensitive. These are however moderate enough that it is still largely the same ion and transitions that are dominant. This gives important robustness to the model predictions. In the bottom panel, model B at 80 d is compared with $f = 3$ and 0.5.

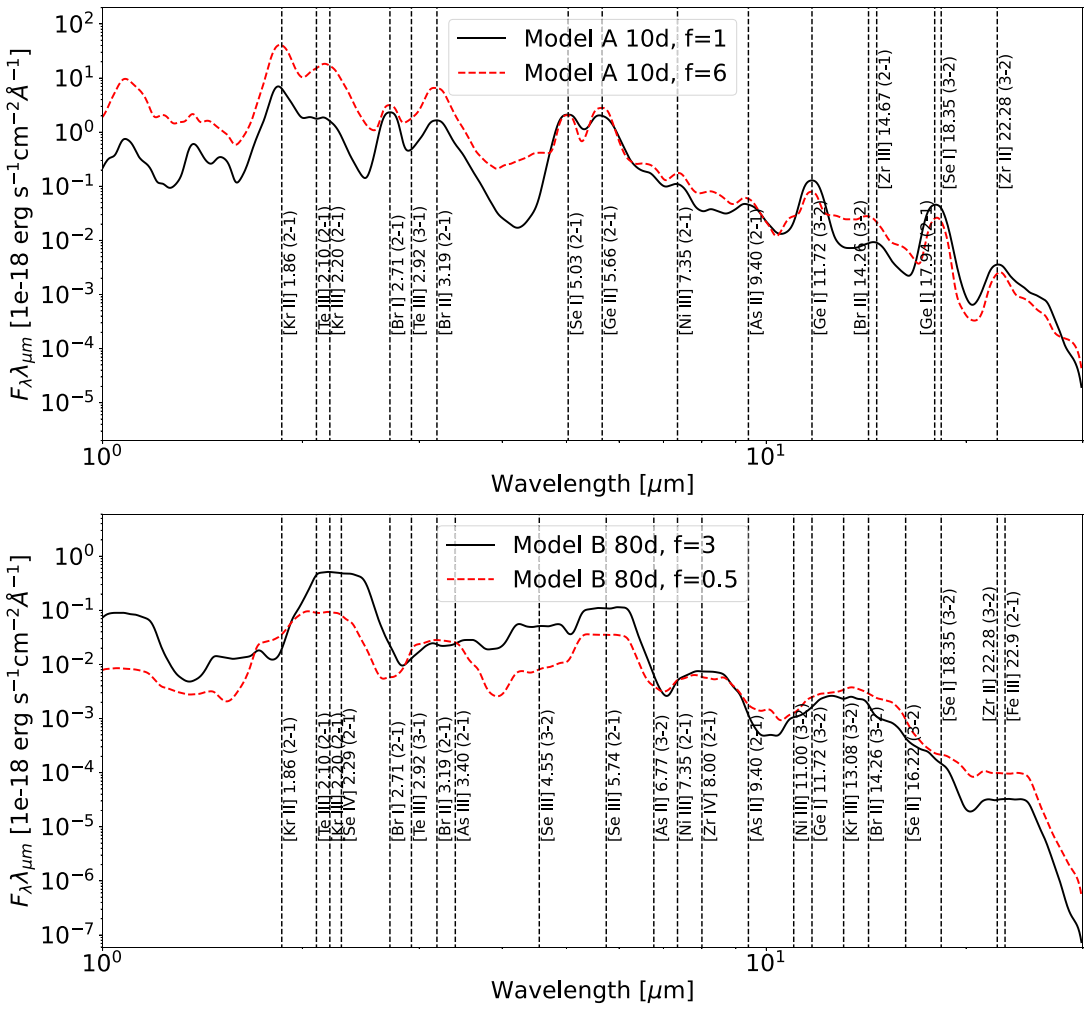

Figure B1. Top: comparison of model A with $f = 1$ and 6, at 10 d. Bottom: comparison of model B with $f = 3$ and 0.5, at 80 d.

APPENDIX C: IONIZATION PROFILES

Figs C1–C6 show the detailed ionization structures in the line-forming regions in the models, for elements with distinct lines.

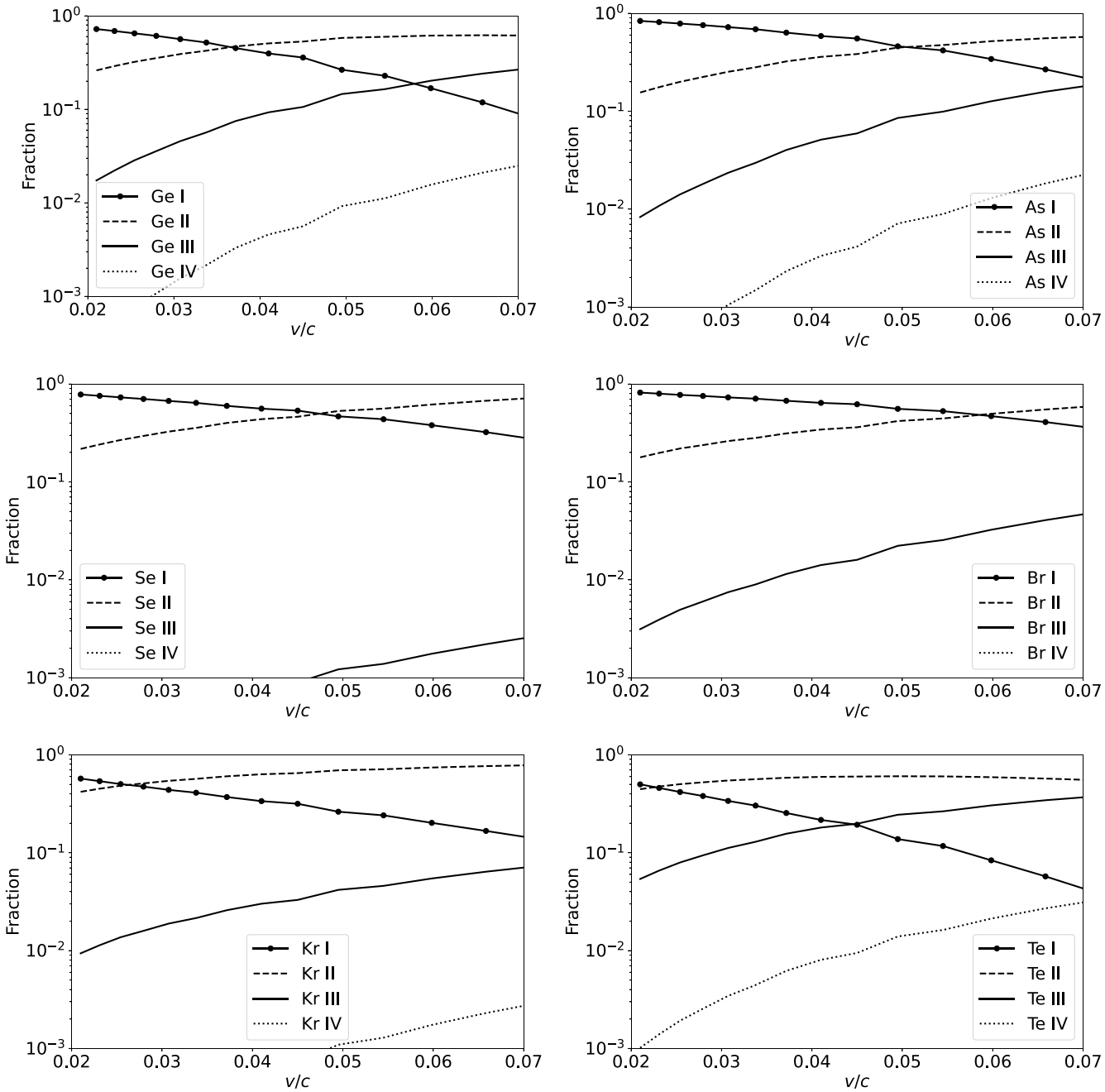

Figure C1. Ionization profiles of selected important elements in model A, at 10 d, zoomed-in on the region $v/c \leq 0.07$ (which has $\gtrsim 80$ per cent of the radioactive energy deposition). Neutral abundances are plotted with solid lines with dots, singly ionized with dashed lines, doubly ionized with solid lines, and triply ionized with dotted lines.

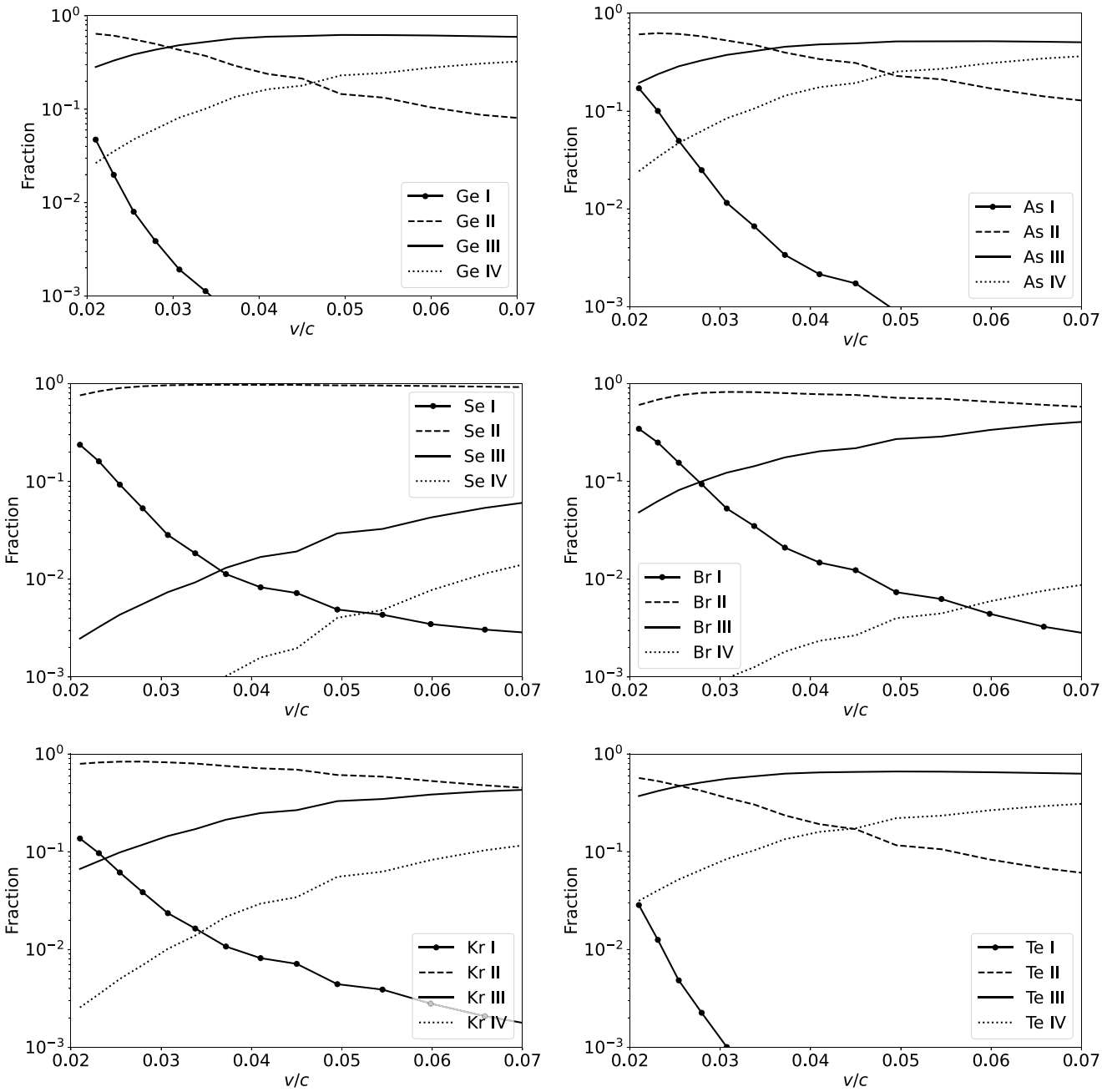

Figure C2. Same as Fig. C1, at 40 d.

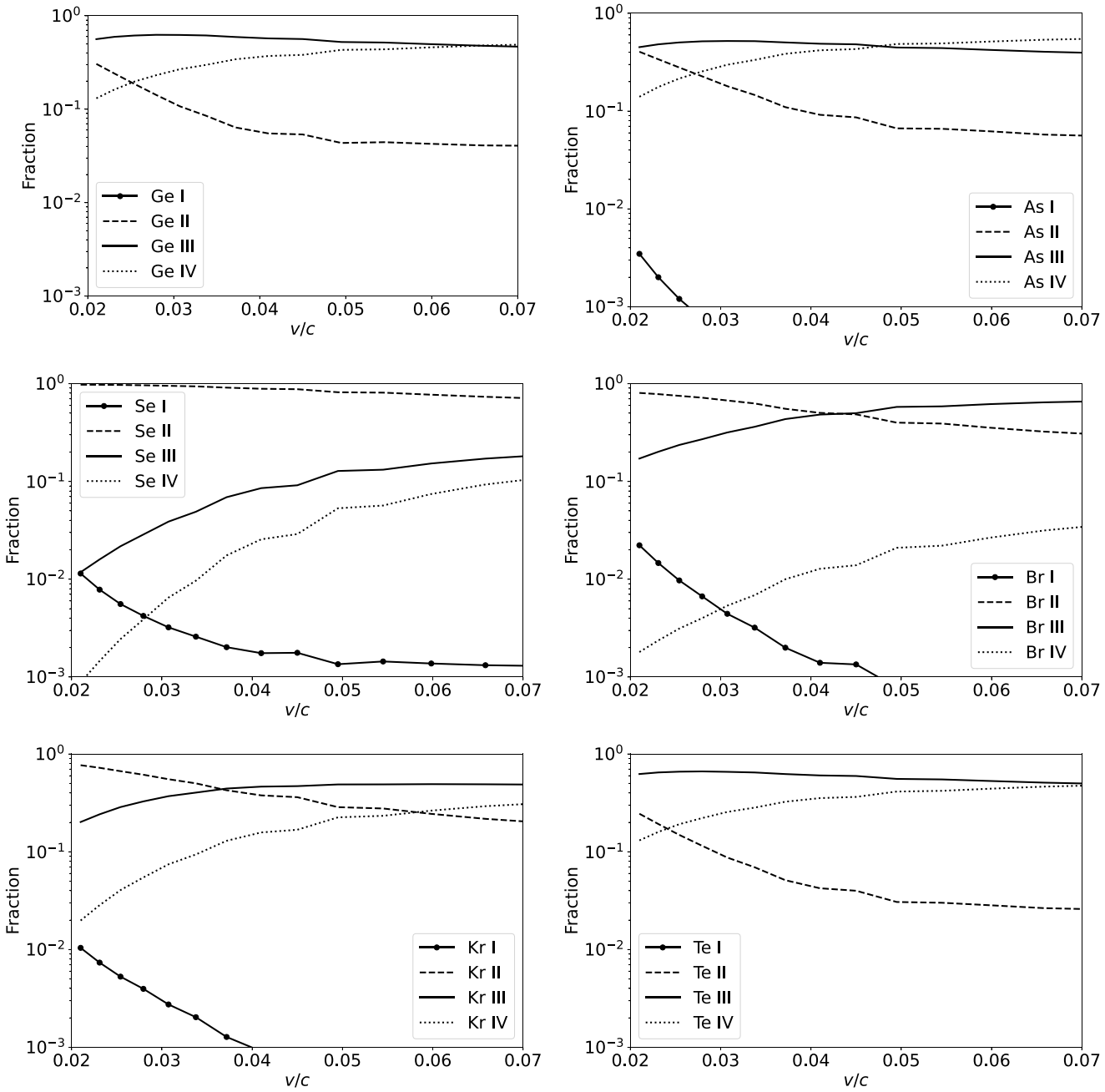

Figure C3. Same as Fig. C1, at 80 d.

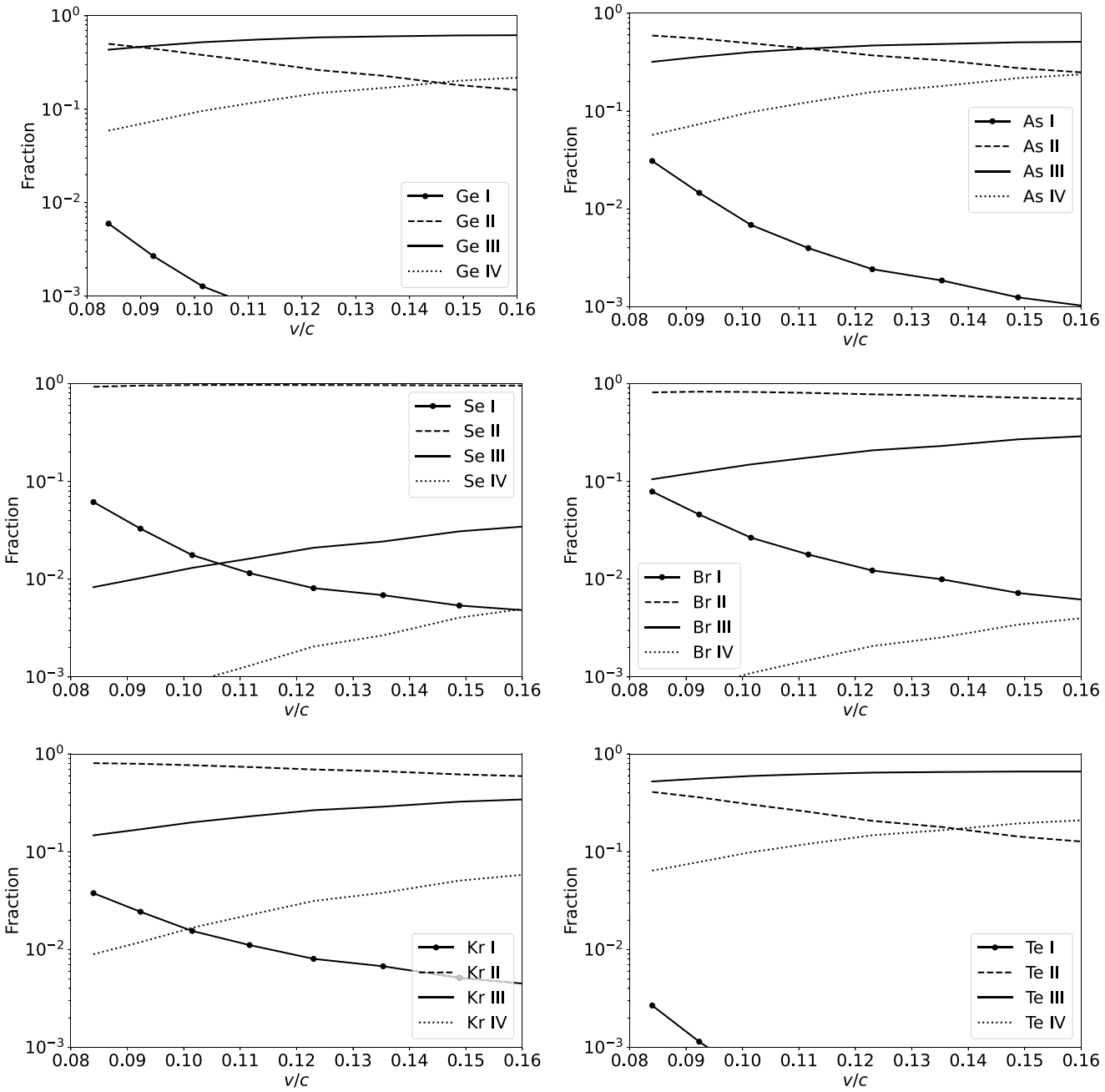

Figure C4. Same as Fig. C1, but model B at 10 d. The inner boundary is here at $v/c = 0.08$ and the $\gtrsim 80$ per cent radioactive deposition limit at $v/c = 0.16$.

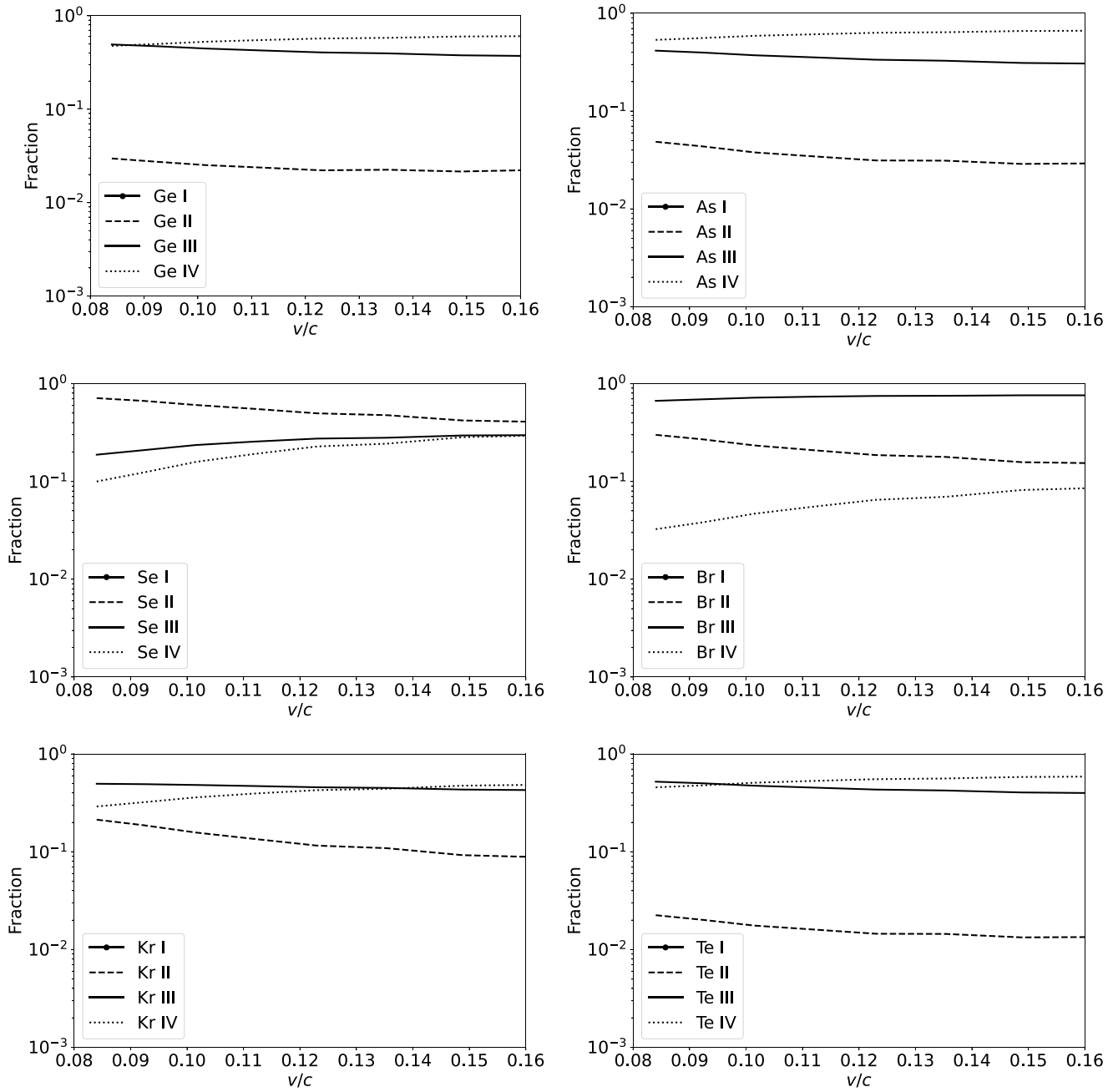

Figure C5. Same as Fig. C4, at 40 d.

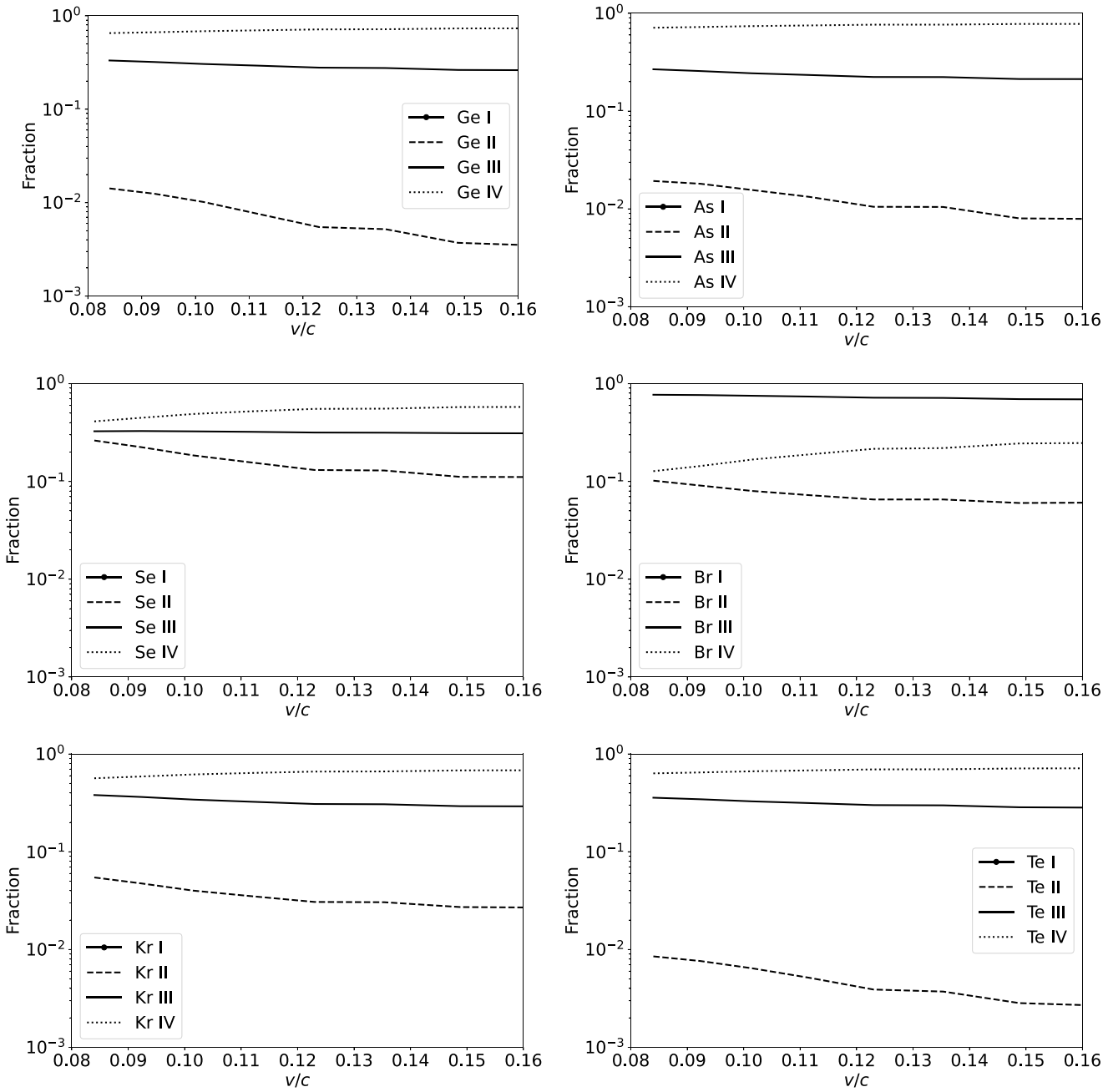

Figure C6. Same as Fig. C4, at 80 d.

This paper has been typeset from a TEX/LATEX file prepared by the author.